

Reverberation Mapping of Two Luminous Quasars: the Broad-line Region Structure and Black Hole Mass

SHA-SHA LI,^{1,2} SEN YANG,^{1,2} ZI-XU YANG,^{1,2} YONG-JIE CHEN,^{1,2} YU-YANG SONGSHENG,^{1,2} HE-ZHEN LIU,^{3,4} PU DU,¹
BIN LUO,^{3,4} ZHE YU,^{1,2} CHEN HU,¹ BO-WEI JIANG,^{1,2} DONG-WEI BAO,^{1,2} WEI-JIAN GUO,^{1,2} ZHI-XIANG ZHANG,⁵ YAN-RONG LI,¹
MING XIAO,¹ KAI-XING LU,⁶ LUIS C. HO,^{7,8} JING-MIN BAI,⁶ WEI-HAO BIAN,⁹ JESÚS ACEITUNO,^{10,11} TAKEO MINEZAKI,¹²
KEITH HORNE,¹³ MITSURU KOKUBO,¹⁴ AND JIAN-MIN WANG^{1,2,15}

¹Key Laboratory for Particle Astrophysics, Institute of High Energy Physics, Chinese Academy of Sciences, 19B Yuquan Road, Beijing 100049, People's Republic of China

²University of Chinese Academy of Sciences, 19A Yuquan Road, Beijing 100049, People's Republic of China

³School of Astronomy and Space Science, Nanjing University, Nanjing, Jiangsu 210093, People's Republic of China

⁴Key Laboratory of Modern Astronomy and Astrophysics(Nanjing University), Ministry of Education, Nanjing, Jiangsu 210093, People's Republic of China

⁵Department of Astronomy, Xiamen University, Xiamen, Fujian 361005, People's Republic of China

⁶Yunnan Observatories, Chinese Academy of Sciences, Kunming 650011, People's Republic of China

⁷Kavli Institute for Astronomy and Astrophysics, Peking University, Beijing 100871, People's Republic of China

⁸Department of Astronomy, School of Physics, Peking University, Beijing 100871, People's Republic of China

⁹Physics Department, Nanjing Normal University, Nanjing 210097, People's Republic of China

¹⁰Centro Astronomico Hispano Alemán, Sierra de los filabres sn, E-04550 GéTablesrgal, Almería, Spain

¹¹Instituto de Astrofísica de Andalucía (CSIC), Glorieta de la astronomía sn, E-18008 Granada, Spain

¹²Institute of Astronomy, School of Science, University of Tokyo, Mitaka, Tokyo 181-0015, Japan

¹³SUPA Physics and Astronomy, University of St. Andrews, North Haugh, KY16 9SS, UK

¹⁴Department of Astrophysical Sciences, Princeton University, Princeton, New Jersey 08544, USA

¹⁵National Astronomical Observatories of China, Chinese Academy of Sciences, 20A Datun Road, Beijing 100020, People's Republic of China

ABSTRACT

We report the results of a multi-year spectroscopic and photometric monitoring campaign of two luminous quasars, PG 0923+201 and PG 1001+291, both located at the high-luminosity end of the broad-line region (BLR) size-luminosity relation with optical luminosities above 10^{45} erg s⁻¹. PG 0923+201 is for the first time monitored, and PG 1001+291 was previously monitored but our campaign has a much longer temporal baseline. We detect time lags of variations of the broad H β , H γ , Fe II lines with respect to those of the 5100 Å continuum. The velocity-resolved delay map of H β in PG 0923+201 indicates a complicated structure with a mix of Keplerian disk-like motion and outflow, and the map of H β in PG 1001+291 shows a signature of Keplerian disk-like motion. Assuming a virial factor of $f_{\text{BLR}} = 1$ and FWHM line widths, we measure the black hole mass to be $118_{-16}^{+11} \times 10^7 M_{\odot}$ for PG 0923+201 and $3.33_{-0.54}^{+0.62} \times 10^7 M_{\odot}$ for PG 1001+291. Their respective accretion rates are estimated to be $0.21_{-0.07}^{+0.06} \times L_{\text{Edd}} c^{-2}$ and $679_{-227}^{+259} \times L_{\text{Edd}} c^{-2}$, indicating that PG 0923+201 is a sub-Eddington accretor and PG 1001+291 is a super-Eddington accretor. While the H β time lag of PG 0923+201 agrees with the size-luminosity relation, the time lag of PG 1001+291 shows a significant deviation, confirming that in high-luminosity AGN the BLR size depends on both luminosity and Eddington ratio. Black hole mass estimates from single AGN spectra will be over-estimated at high luminosities and redshifts if this effect is not taken into account.

Keywords: Quasars(1319); Supermassive black holes (1663); Reverberation mapping (2019)

1. INTRODUCTION

Over the past four decades, reverberation mapping (RM) technique (Bahcall et al. 1972; Blandford & McKee 1982; Peterson 1993, 2014) has been established as a standard tool for measuring the mass of the central supermassive black hole (SMBH) and for studying geometry and dynamics of the broad-line region (BLR) in active galactic nuclei (AGNs). The characteristic

time delay τ_{BLR} between broad emission line and continuum variations corresponds to the light traveling time from the central continuum source to the BLR, and therefore implies the BLR size by multiplying the time delay with the light speed, namely, $R_{\text{BLR}} = c \tau_{\text{BLR}}$. Assuming the BLR is virialized, the black hole mass can be determined through R_{BLR} and the broad emission-line width ΔV ,

$$M_{\bullet} = f_{\text{BLR}} \frac{R_{\text{BLR}} \Delta V^2}{G}, \quad (1)$$

where G is the gravitational constant and f_{BLR} is the so-called virial factor depending on geometry and kinematics of the BLR (e.g., Ho & Kim 2014).

Up to now, there are about a hundred AGN RM observations and black hole mass measurements (e.g., Peterson et al. 1998, 2002, 2004; Kaspi et al. 2000; Bentz et al. 2008, 2009; Denney et al. 2009, 2010; Barth et al. 2011, 2013, 2015; Grier et al. 2012, 2017; Du et al. 2014, 2015, 2016b, 2018a,b; Shen et al. 2016; Fausnaugh et al. 2017; De Rosa et al. 2018; Huang et al. 2019; Lu et al. 2019; Zhang et al. 2019; Hu et al. 2020a,b, 2021). Those RM observations have established the widely used $R_{\text{H}\beta} - L_{5100}$ relation between the size of $\text{H}\beta$ BLR ($R_{\text{H}\beta}$) and the monochromatic luminosity at 5100 Å (L_{5100}) (e.g., Kaspi et al. 2000; Peterson & Wandel 1999, 2000; Bentz et al. 2013), which allows us to infer BLR sizes with single-epoch spectra and therefore to economically estimate black hole masses for large AGN samples. Needless to say, to reliably estimate black hole masses in single-epoch observations, the RM sample used for building up the $R_{\text{H}\beta} - L_{5100}$ relation needs to cover a variety of AGN populations. Recent RM campaigns indeed show that $\text{H}\beta$ time lags of super-Eddington accreting AGNs deviate from the $R_{\text{H}\beta} - L_{5100}$ relation (Du et al. 2015, 2016b, 2018b; Fonseca Alvarez et al. 2020).

On the other hand, due to the intensive time demands of RM observations, most of the previous RM campaigns were concentrated on low-luminosity and low-redshift sources. Time delays of those sources are relatively short (days or weeks) and the required monitoring periods are only several months. By contrast, RM of high-luminosity and high-redshift AGNs suffers the following restrictions. First, optical variability of high-luminosity AGNs is generally weak (e.g., Hook et al. 1994; Giveon et al. 1999; Vanden Berk et al. 2004; Kelly et al. 2009), imposing difficulties on RM monitoring. Second, time delays for higher-redshift and higher-luminosity AGN are generally longer and monitoring periods are accordingly needed to be extended to years. Third, for high-redshift AGNs ($z \gtrsim 0.7$), $\text{H}\beta$ emission lines are redshifted out of optical bands and infrared RM is required. Unfortunately, there has not been such infrared RM campaigns for $\text{H}\beta$ yet. Hitherto, there are only a few RM sources at the high-luminosity ($L_{5100} > 10^{45} \text{ erg s}^{-1}$) end of the $R_{\text{H}\beta} - L_{5100}$ relation. In this regard, it is quite necessary to expand the high-luminosity RM sample.

To this end, we undertook a multi-year RM campaign on two luminous quasars, PG 0923+201 and PG 1001+291, both with an optical luminosity above $10^{45} \text{ erg s}^{-1}$. The obtained data allow us to measure the time delays of the broad $\text{H}\beta$, $\text{H}\gamma$, and Fe II lines as well as to constrain the BLR kinematics of the broad $\text{H}\beta$ line.

The paper is organized as follows. Observations and data reduction are described in Section 2. In Section 3, we explain in detail measurements of light curves of continuum and broad emission lines as well as intercalibrations of continuum light curves from our campaign and other time-domain survey archives. In Section 4, we present the time delay analysis and black hole mass measurements. In Section 5, we discuss the implication of our results on the $R_{\text{H}\beta} - L_{5100}$ relation and the location of PG 0923+201 in the main sequence of RM samples. Here, the main sequence refers to the relation between full widths at half maximum (FWHMs) of broad $\text{H}\beta$ lines and strengths of Fe II (\mathcal{R}_{Fe}), where \mathcal{R}_{Fe} is the flux ratio of Fe II emission lines between 4434 Å and 4684 Å to broad $\text{H}\beta$ lines. The conclusions are summarized in Section 6. Throughout the paper, we use a Λ CDM cosmology with $H_0 = 67 \text{ km s}^{-1} \text{ Mpc}^{-1}$, $\Omega_{\text{M}} = 0.32$, and $\Omega_{\Lambda} = 0.68$ (Planck Collaboration et al. 2020).

2. OBSERVATIONS AND DATA REDUCTION

2.1. Targets

We spectroscopically monitored two quasars, PG 0923+201 and PG 1001+291, both with an optical luminosity larger than $10^{45} \text{ erg s}^{-1}$. Their basic properties are summarized below.

PG 0923+201 has a redshift of $z = 0.1921$, $m_{\text{g}} = 15.6 \text{ mag}$, and V -band extinction $A_{\text{V}} = 0.116 \text{ mag}$ (Schlafly & Finkbeiner 2011). Its spectrum shows prominent Fe II emission lines, and weak [O III] $\lambda 5007$ line (Boroson & Green 1992). The ratios of the equivalent width of [O III] $\lambda 5007$ and Fe II between 4434 Å and 4684 Å to that of $\text{H}\beta$ are about 0.04 and 0.72, respectively. Such strong Fe II and weak [O III] emission lines are common features seen in narrow-line Seyfert 1 galaxies (NLS1s), which are generally believed to be accreting at a super-Eddington rate. However, the FWHM of the $\text{H}\beta$ line is as large as $\sim 7600 \text{ km s}^{-1}$, much broader than NLS1s (usually narrower than 2000 km s^{-1}).

PG 1001+291 has a redshift of $z = 0.3272$, $m_{\text{g}} = 15.9 \text{ mag}$, and $A_{\text{V}} = 0.06 \text{ mag}$ (Schlafly & Finkbeiner 2011). Similar to PG 0923+201, PG 1001+291 also shows prominent Fe II emission lines with $\mathcal{R}_{\text{Fe}} \sim 1.17$ and weak [O III] line (Du & Wang

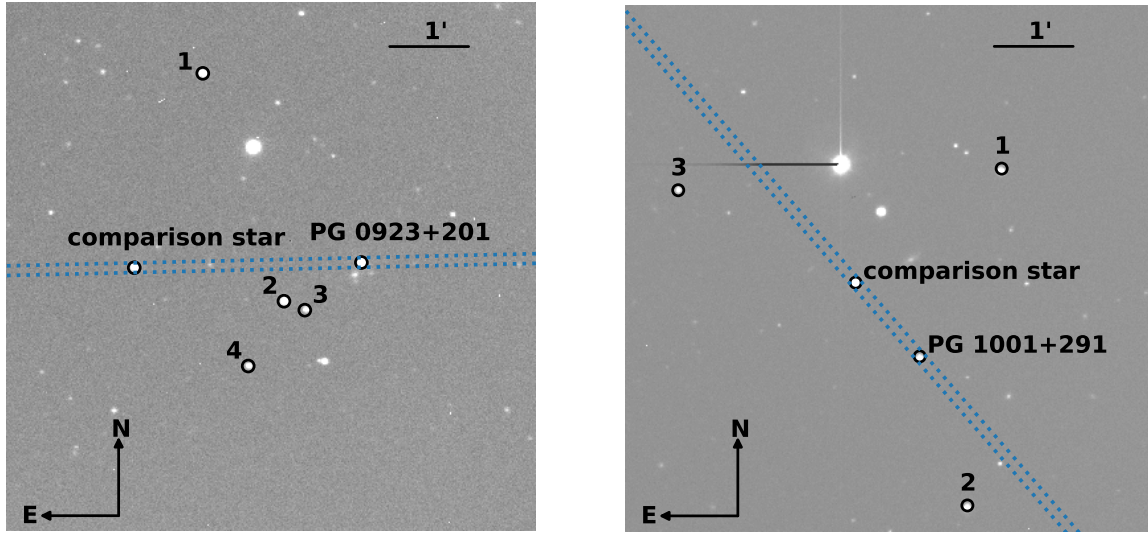


Figure 1. Images of PG 0923+201 (left) and PG 1001+291 (right) and their comparison stars. Stars 1-4 in the image of PG 0923+201 and stars 1-3 in the image of PG 1001+291 are selected for differential photometry. The blue dotted lines illustrate the directions of slits.

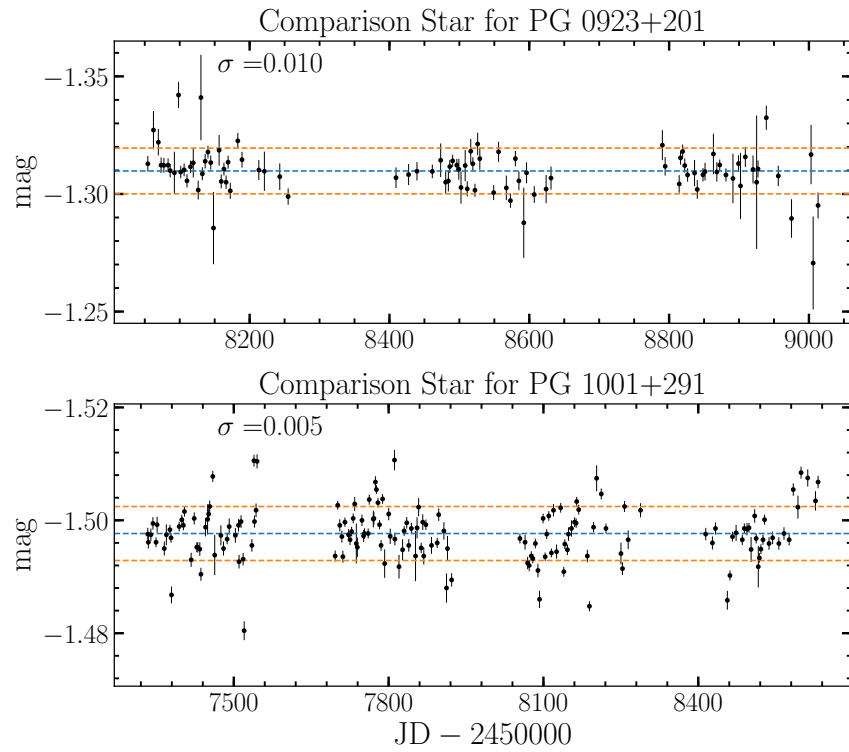


Figure 2. Photometric light curves of the comparison stars for PG 0923+201 (top) and PG 1001+291 (bottom), in units of instrumental magnitudes. Blue dashed lines represent the mean magnitudes and orange dashed lines represent the standard deviations.

2019). However, its $H\beta$ line has a much narrower FWHM, only about 2100 km s^{-1} . PG 1001+291 was monitored between 2015 and 2017 by the Super-Eddington Accreting Massive Black Holes (SEAMBH) campaign¹ (Du et al. 2018b, who used the

¹ The selection criteria for SEAMBHs were: strong optical Fe II, relatively narrow $H\beta$, and weak [O III] lines (see Du et al. 2014, 2018b).

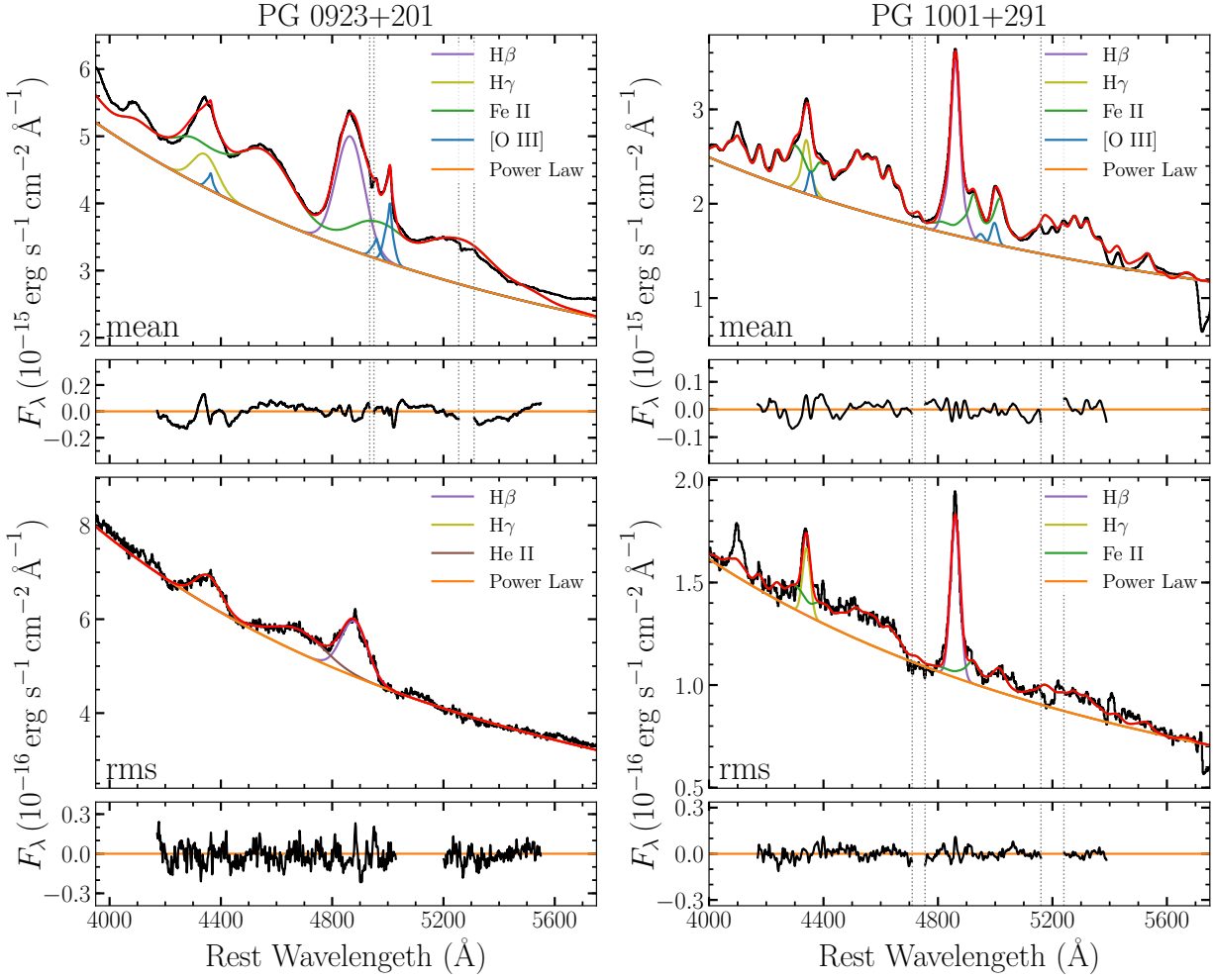


Figure 3. Spectral decompositions of the mean spectrum (top) and the rms spectrum (bottom) for PG 0923+201 in left panels and PG 1001+291 in right panels. In each case, two vertical adjacent panels show the details of spectral decompositions and the residuals in fitting windows. The vertical dotted lines indicate the regions omitted from the fits.

alternative SDSS name for PG 1001+291, namely, SDSS J100402.61+285535.3). The $H\beta$ lag ($32.2^{+43.5}_{-4.2}$ days) was relatively uncertain due to the short monitoring period. Nevertheless, the $H\beta$ lag of PG 1001+291 was found to be 0.80 dex below the $R_{H\beta} - L_{5100}$ relation (Du et al. 2018b).

2.2. Spectroscopy

In our observations, spectroscopy was mainly undertaken with the Lijiang 2.4 m telescope at the Yunnan Observatories of Chinese Academy of Sciences. It is equipped with the Yunnan Faint Object Spectrograph and Camera (YFOSC) that can switch quickly between spectroscopy and photometry modes. The observations and data reduction were carried out following Du et al. (2014, 2015). We briefly summarize important points about observation setup below. (1) For PG 0923+201, the spectra were obtained by Grism 14 with a dispersion of $1.78 \text{ \AA pixel}^{-1}$ and a wavelength coverage of $3800 - 7400 \text{ \AA}$. We used a long slit with a projected width of $2.''5$. The instrumental broadening was about 500 km s^{-1} (in terms of FWHM; Du et al. 2014). (2) For PG 1001+291, due to its larger redshift, Grism 14 would induce contamination of the second-order spectrum at the observed-frame wavelength longer than 6600 \AA (see Lu et al. 2019; Feng et al. 2021). We therefore used Grism 3 to avoid the contamination. Grism 3 has a spectral coverage of $3800 - 9000 \text{ \AA}$ and a dispersion of $2.9 \text{ \AA pixel}^{-1}$. We adopted a $5.''0$ wide slit and the instrumental broadening is about 1200 km s^{-1} (Du et al. 2015).

For each target, we rotated the slit to cover a selected comparison star simultaneously for flux calibration (see Figure 1). We selected the comparison star WISEA J092607.03+195357.5 for PG 0923+201 and WISEA J100406.45+285631.6 for PG 1001+291. The spectroscopic images were reduced using standard IRAF procedures. A uniform aperture of $8.''5$ and a

Table 1. Properties of spectral and photometric data

Object	Source	Monitoring Period		Epochs	ΔT (day)
		JD - 2457000	Date		
PG 0923+201	LJS	1054 – 1975	2017 Oct – 2020 May	89	5.9
	LJP	1054 – 2013	2017 Oct – 2020 Jun	85	6.0
	ASAS-SN	298 – 2021	2015 Oct – 2020 Jun	519	1.7
	ZTF	1202 – 2000	2018 Mar – 2020 May	374	0.1
PG 1001+291	LJS	334 – 1632	2015 Nov – 2019 May	164	4.9
	LJP	333 – 1632	2015 Nov – 2019 Jun	160	4.1
	ZTF	1202 – 1649	2018 Mar – 2019 Jun	143	1.0
	CAHAS	894 – 1492	2017 May – 2019 Jan	16	11.9
	CAHAP	909 – 1492	2017 Jun – 2019 Jan	14	11.1

NOTE—LJS and CAHAS refer to spectroscopy from Lijiang and CAHA. LJP, CAHAP, ASAS-SN, and ZTF refer to photometry from Lijiang, CAHA, ASAS-SN archive, and ZTF archive, respectively. ΔT refers to the median sampling interval.

background region of $7.''4 - 14''$ were used for spectrum extraction. Two consecutive 1200 s exposures were taken on each observing night. For PG 0923+201, we obtained a total of 89 epochs of spectroscopic observations between October 2017 and May 2020. For PG 1001+291, we obtained a total of 164 epochs between November 2015 and May 2019. The median sampling intervals of PG 0923+201 and PG 1001+291 are 5.9 and 4.9 days, respectively (see Table 1). For each night, the typical signal-to-noise ratio (S/N) per pixel at 5100 Å (rest frame) is ~ 57 for PG 0923+201 and ~ 48 for PG 1001+291.

Since May 2017, PG 1001+291 was also observed with the Centro Astronómico Hispano-Alemán (CAHA) 2.2 m telescope at the Calar Alto Observatory in Spain (see Hu et al. 2020a,b). The spectra were taken with the Calar Alto Faint Object Spectrograph (CAFOS) using the same observation strategy described above. The adopted Grism G-200 has a dispersion of $4.47 \text{ \AA pixel}^{-1}$ and a spectral coverage of 4000 – 8500 Å. We used a long slit with a projected width of $3.''0$ and the resulting instrumental broadening is about 1000 km s^{-1} (Hu et al. 2020b). We selected the same comparison star as in our Lijiang observations. A uniform aperture of $10.''6$ and a background region of $13.''8 - 26.''5$ were used for spectrum extraction (see Hu et al. 2020b for data reduction details). In total, we obtained 16 epochs between May 2017 and January 2019 at the Calar Alto Observatory. The typical S/N per pixel at 5100 Å (rest frame) is ~ 68 of each night.

The Fe II blends are relatively strong beneath the [O III] line and the [O III] $\lambda 5007$ line is too weak to apply [O III]-based calibration (van Groningen & Wanders 1992). Therefore, we adopt the method based on comparison stars, which provides sufficiently accurate flux calibration (Maoz et al. 1990; Du et al. 2018b). Because the target and its comparison star are observed simultaneously, their emitted lights travel along the same path and thereby suffer the same seeing and atmospheric conditions. This enables high-accuracy relative flux measurements even in relatively poor weather conditions. The calibration steps are as follows. First, we use the spectrophotometric standard stars to calibrate the absolute spectra of the comparison star observed on several good-weather nights. We average these calibrated spectra of the comparison star to generate a fiducial spectrum. Second, in each observation, we compare the comparison star’s spectrum with the fiducial spectrum to get a sensitivity function, and use this sensitivity function to calibrate the target’s spectrum. We note that the absolute spectrum of the comparison star is not important, because RM analysis only depend on relative flux variations. Below, we also illustrate that the selected comparison stars are stable in photometry and therefore suitable for flux calibration. Figure 1 plots images to illustrate sky locations of the two quasars and their comparison stars along with slits.

2.3. Photometry

Photometry was obtained directly through the image mode of YFOSC. We used the Johnson V filter and SDSS r' -band filter for PG 0923+201 and PG 1001+291, respectively. Typically we took three 50 s exposures for each object on each observing night. We used standard IRAF procedures to reduce the photometric data. Several stars were selected in the $10' \times 10'$ field of view for differential photometry (see Figure 1). According to aperture tests, we found that a circular aperture with a radius of $4.''5$ and $4.''2$ provides the best photometry for the two objects, respectively. The inner and outer radius of the background was uniformly set to be $8.''5 - 17''$. Figure 2 shows the photometric light curves of the comparison stars over our monitoring periods,

Table 2. Light curves of PG 0923+201

Spectra					Photometry		
JD - 2450000	F_{5100}	$F_{H\beta}$	$F_{H\gamma}$	Obs.	JD - 2450000	mag	Obs.
8054.37	26.45 ± 0.37	21.46 ± 0.33	5.74 ± 0.19	L	7298.12	15.457 ± 0.086	A
8065.37	26.48 ± 0.38	21.84 ± 0.36	5.71 ± 0.22	L	7299.12	15.397 ± 0.078	A
8069.43	26.81 ± 0.36	20.86 ± 0.31	5.44 ± 0.17	L	7308.11	15.416 ± 0.054	A
8073.35	27.75 ± 0.37	21.12 ± 0.32	5.86 ± 0.19	L	7310.11	15.464 ± 0.062	A
8077.37	27.47 ± 0.37	20.92 ± 0.32	5.56 ± 0.19	L	7311.11	15.482 ± 0.058	A

NOTE—The 5100 Å continuum flux densities are in units of 10^{-16} erg s $^{-1}$ cm $^{-2}$ Å $^{-1}$, and the fluxes of emission lines are in units of 10^{-14} erg s $^{-1}$ cm $^{-2}$. In the “Obs.” column, “L” refers to Lijiang, “A” refers to ASAS-SN, and “Z” refers to ZTF.

(This table is available in its entirety in a machine-readable form in the online journal.)

both of which have a standard deviation $\lesssim 0.01$ mag, indicating that the comparison stars were stable enough for flux calibration. We finally obtained a total of 85 and 160 epochs of photometric observations for PG 0923+201 and PG 1001+291 with median sampling intervals of 6.0 and 4.1 days, respectively (see Table 1). Tables 2 and 3 list photometric light curves of the two targets.

We also obtained photometry of PG 1001+291 using the CAFOS image mode with a Johnson V filter at the Calar Alto Observatory. Typically, three 60 s exposures were taken on each observing night. The photometry was reduced using standard IRAF procedures with the same configurations as in our Lijiang observations. We secured 14 epochs between June 2017 and January 2019 at the Calar Alto Observatory.

Besides our observations, we compiled photometry from archived data of the All-Sky Automated Survey for Supernovae (ASAS-SN) and the Zwicky Transient Facility (ZTF).

The ASAS-SN² is a long-term project designed to survey the whole visible sky every night down to about 17 magnitude to discover nearby supernovae and other transient sources (Shappee et al. 2014; Kochanek et al. 2017). The ASAS-SN project is composed of multiple stations, each station containing a 14 cm Nikon telephoto lenses equipped with a thermo-electrically cooled CCD camera. The field of view of each camera is about 4.5 deg², and the pixel scale is 8″. Observations generally used V or g band filters for three dithered 90s exposures. The photometric data were processed using IRAF apphot package with an aperture radius of 16″ and calibrated according to AAVSO Photometric All-Sky Survey (Henden et al. 2012). For PG 0923+201, there are 519 epochs with a median sampling interval of 1.7 days from October 2015 to June 2020 (see Table 1). For PG 1001+291, the ASAS-SN data are not adopted because of the relatively poor data quality.

The ZTF³ is designed for transients and variables and uses the Palomar 48-inch Schmidt Telescope with a 47 square degree field of view and a 600 megapixel camera to scan the entire northern visible sky (Bellm et al. 2019; Graham et al. 2019; Masci et al. 2019). The ZTF provides two filters ZTF- g and ZTF- r , with the median photometric depths down to 20.8 and 20.6 mag, respectively. We combine the light curves of ZTF- g and ZTF- r bands using the intercalibration method described in Section 3.2. There are 374 epochs with typically 3 observations per night between March 2018 and May 2020 for PG 0923+201 and 143 epochs with a median sampling interval of 1.0 days from March 2018 to June 2019 for PG 1001+291 (see Table 1).

3. MEASUREMENTS

3.1. Light Curves

We measure the 5100 Å flux density and broad $H\beta$ line via a multi-component spectral fitting scheme (SFS) following Hu et al. (2015, 2020a,b). Before fitting, we correct the Galactic extinction using the extinction law of Cardelli et al. (1989) with $R_V = 3.1$. We employ the DASpec⁴ software to perform multi-component spectral fitting. The software uses the Levenberg-Marquardt method to minimize the chi-square. The details of the fitting procedures for the two targets are slightly different, as described below.

² <http://www.astronomy.ohio-state.edu/asassn/index.shtml>

³ <https://www.ztf.caltech.edu>

⁴ DASpec is available at <https://github.com/PuDu-Astro/DASpec>.

Table 3. Light curves of PG 1001+291

Spectra						Photometry		
JD - 2450000	F_{5100}	$F_{H\beta}$	$F_{H\gamma}$	$F_{Fe\ II}$	Obs.	JD - 2450000	mag	Obs.
7334.41	15.32 ± 0.11	8.60 ± 0.11	2.36 ± 0.10	11.20 ± 0.23	L	7333.42	15.944 ± 0.003	L
7339.40	14.78 ± 0.12	8.65 ± 0.13	2.20 ± 0.11	11.38 ± 0.27	L	7334.40	15.945 ± 0.003	L
7343.34	14.70 ± 0.13	8.29 ± 0.14	2.34 ± 0.12	11.13 ± 0.29	L	7339.38	15.956 ± 0.003	L
7349.38	15.11 ± 0.10	8.49 ± 0.07	2.41 ± 0.06	10.71 ± 0.15	L	7343.33	15.962 ± 0.003	L
7351.42	14.96 ± 0.11	8.72 ± 0.10	2.31 ± 0.08	11.38 ± 0.19	L	7349.37	15.970 ± 0.002	L

NOTE—The 5100 Å continuum flux densities are in units of 10^{-16} erg s $^{-1}$ cm $^{-2}$ Å $^{-1}$, and the fluxes of emission lines are in units of 10^{-14} erg s $^{-1}$ cm $^{-2}$. In the “Obs.” column, “L” refers to Lijiang, “C” refers to CAHA, and “Z” refers to ZTF. (This table is available in its entirety in a machine-readable form in the online journal.)

PG 0923+201—There is no obvious stellar absorption feature in our spectra (see Figure 3; near ~ 4940 and 5280 Å are telluric absorptions), so we do not add a host galaxy template in the fitting. The fitting components include: (1) a single power law, (2) an Fe II template from Boroson & Green (1992), (3) a single Gaussian for broad emission lines H β , H γ , (4) double Gaussians for [O III] $\lambda\lambda 4959, 5007$ and [O III] $\lambda 4363$ with the same tied velocity shifts and widths among the three line. The narrow H β is not added because the flux of the narrow H β is less than 2% of the total H β flux, and the narrow H β flux is estimated by assuming that a typical flux ratio of 0.1 between the narrow H β and [O III] $\lambda 5007$ (e.g., Veilleux & Osterbrock 1987; Hu et al. 2015).

Because the H γ is blended with [O III] $\lambda 4363$, we fix the velocity width and shift of H γ to those of H β . The flux ratio of [O III] $\lambda 4363$ relative to [O III] $\lambda 5007$ is fixed to 0.251 obtained by the best fit of the mean spectrum. The [O III] lines have asymmetric blue wings, which is seen more clearly in the high-resolution spectrum from the Sloan Digital Sky Survey (SDSS). We therefore apply two Gaussians to fit the [O III] lines, one of which is set to be narrower and the other is set to broader. The width and shift of the broader Gaussian component of [O III] lines are fixed to the value obtained via the best fit to the SDSS spectrum after considering the different instrumental broadening of SDSS and Lijiang telescope. The fitting is performed at 4170–5550 Å excluding the telluric absorption windows around 4940 Å and 5280 Å.

We note that although the He II $\lambda 4686$ line is relatively prominent in the root mean square (rms) spectrum, it is weak and highly blended with the Fe II and the blue wing of the H β in individual spectra so that it cannot be well constrained in the SFS. We therefore do not include a He II component. To evaluate the influences of the He II line on the time delay measurements, we present the results by adding a Gaussian to account for the He II component in Appendix A. The obtained time delays from the two schemes are consistent within uncertainties, indicating that the influences of the He II line are minor.

PG 1001+291—Again, the host galaxy template is not included. The fitting components include: (1) a single power law, (2) a Fe II template from Boroson & Green (1992), (3) a fourth-order Gauss-Hermite function for broad H β and broad H γ , (4) a single Gaussian with the same velocity width and shift for narrow lines [O III] $\lambda\lambda 4959, 5007$ and [O III] $\lambda 4363$. Similar to PG 0923+201, the width and shift of H γ are fixed to those of H β , and the flux ratio of [O III] $\lambda 4363$ to [O III] $\lambda 5007$ is fixed to the fitted value of the mean spectrum. The fitting is performed at 4170–5390 Å, excluding the telluric absorption windows around 4730 Å and 5200 Å (see Figure 3).

The light curves of the continuum flux density at 5100 Å (F_{5100}) and the broad emission lines (H β and H γ of PG 0923+201; H β , H γ , and Fe II of PG 1001+291) are directly obtained from the above fitting and summarized in Tables 2 and 3. The reported errors of the light curves include the Poisson errors and additional systematic errors (added in quadrature). The additional systematic errors are determined following the procedure described in Du et al. (2014). We note that the current Fe II data of PG 0923+201 is not enough to detect a reliable time delay so that we do not present Fe II analysis for PG 0923+201 in this work.

3.2. Intercalibration

We merge the photometric data from our observations, the ASAS-SN, and the ZTF into the 5100 Å continuum to obtain a combined continuum light curve. Time lags between different bands are typically of days (e.g., Edelson et al. 2019), far smaller than the time lags of broad emissions, therefore, such an intercalibration is feasible and does not affect the final time lag measurements. Due to inhomogeneous apertures, the photometric and 5100 Å continuum data need intercalibration, namely, applying

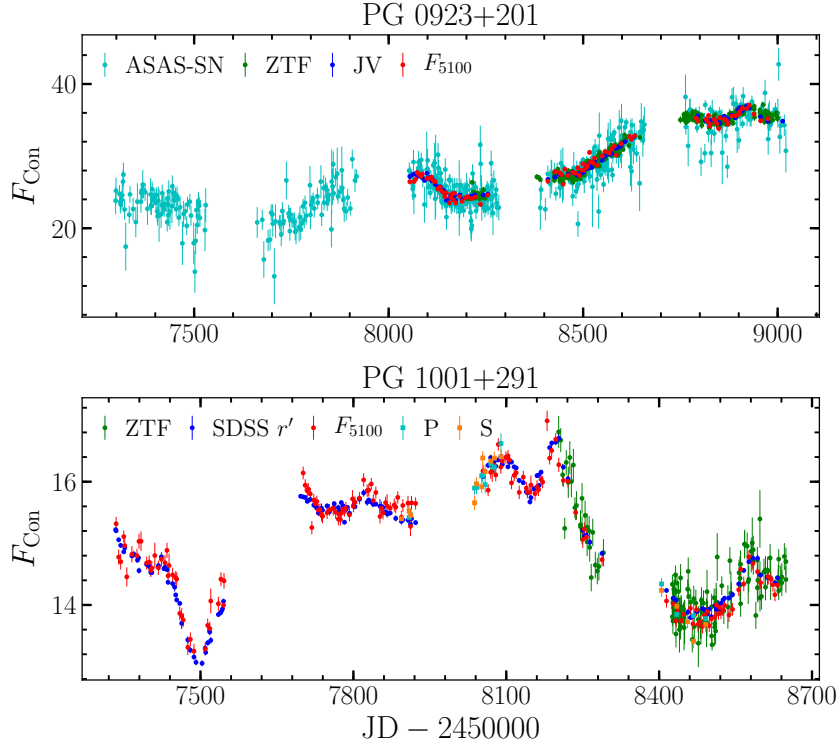


Figure 4. The intercalibrated continuum light curves that combine the 5100 Å continuum (F_{5100}), and photometry from our Lijiang observations (JV/SDSS r') and ASAS-SN and ZTF archives. “P” and “S” refer to photometric data and 5100 Å continuum from CAHA observations, respectively.

additive and multiplicative factors to bring different light curves into a common scale. We use the Python package PyCALI⁵, which employs a Bayesian framework to do intercalibration (see details in Li et al. 2014). The intercalibrated continuum light curves are shown in Figure 4. For PG 1001+291, the ASAS-SN data are not used (see Section 2.3). After intercalibration, we further rebin the continuum light curves by one day apart to combine measurements on the same night. The finally rebinned continuum light curves are used to measure time lags, shown in the panel (a) of Figures 5 and 6.

For PG 1001+291, we obtained spectra from both Lijiang and CAHA observations, therefore, an intercalibration of the spectra is also required. Since the instrumental broadening width (in terms of FWHM) of Lijiang and CAHA observations are roughly similar and far smaller than broad line widths, there is no need to adjust the spectral resolutions. We simply use the intercalibration factors obtained above to align fluxes of the spectra. In the panels (b)-(d) of Figure 6, we show the intercalibrated light curves of emission lines for PG 1001+291 with Lijiang data in black and CAHA data in blue.

3.3. Variability Characteristics

As usual, we calculate quantities F_{var} and R_{max} to measure the intrinsic variability amplitudes (Rodríguez-Pascual et al. 1997). Here, R_{max} is the ratio of maximum to minimum fluxes of the light curve, and F_{var} is defined as

$$F_{\text{var}} = \frac{(S^2 - \Delta^2)^{1/2}}{\bar{F}}, \quad (2)$$

where S^2 is the sample variance, Δ^2 is the mean square error, and \bar{F} is the sample mean flux

$$S^2 = \sum_{i=1}^N \frac{(F_i - \bar{F})^2}{(N-1)}, \quad \Delta^2 = \sum_{i=1}^N \frac{\Delta_i^2}{N}, \quad \bar{F} = \sum_{i=1}^N \frac{F_i}{N}, \quad (3)$$

⁵ PyCALI is available at <https://github.com/LiyAstroph/PyCALI>.

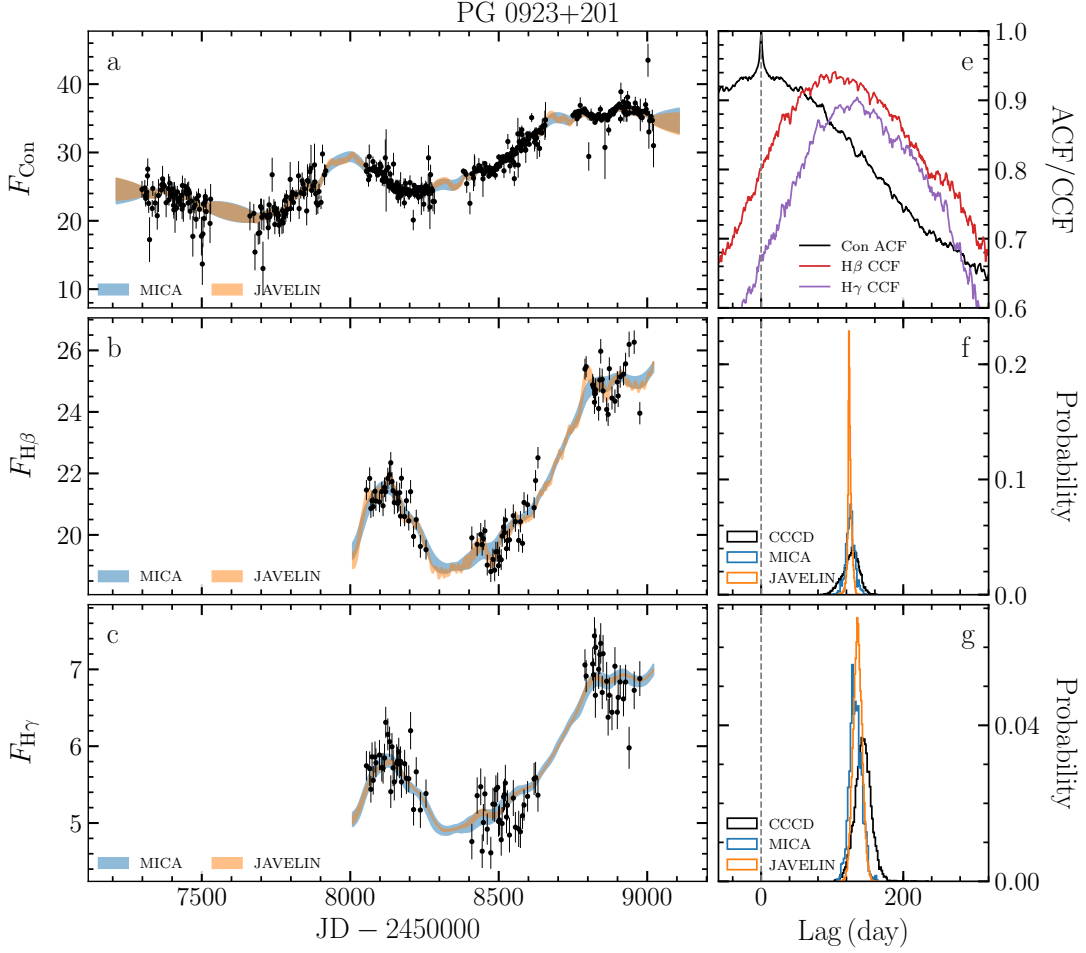


Figure 5. Left panels show the light curves of the combined continuum (a) and broad emission lines (b)-(c). Superposed are the reconstructions by JAVELIN (in orange) and MICA (in blue). The units of the continuum and emission line light curves are $10^{-16} \text{ erg s}^{-1} \text{ cm}^{-2} \text{ \AA}^{-1}$ and $10^{-14} \text{ erg s}^{-1} \text{ cm}^{-2}$, respectively. Right panels show time lag analysis. Panel (e) plots the ACF of the combined continuum, and the CCFs between the broad emission lines with continuum light curves. Panels (f)-(g) show the distributions of time delays for the broad emission lines.

where F_i is the flux of i th observation, Δ_i is the uncertainty of F_i , and N is the total number of epochs. The standard deviation of F_{var} is estimated by (Edelson et al. 2002)

$$\sigma_{\text{var}} = \frac{1}{F_{\text{var}}} \left(\frac{1}{2N} \right)^{1/2} \frac{S^2}{\bar{F}^2}. \quad (4)$$

The variability characteristics of our light curves are given in Table 4. The variability amplitudes of the emission lines for both PG 0923+201 and PG 1001+291 can be ranked in the following order: $\text{H}\gamma > \text{H}\beta$, $\text{H}\gamma > \text{H}\beta > \text{Fe II}$. Such variability ranks are commonly seen in previous observations (e.g., Bentz et al. 2010; Barth et al. 2015; Hu et al. 2020a,b). The mean fluxes of combined continuum and broad emission lines are also listed in Table 4.

4. ANALYSIS AND RESULTS

4.1. Time Lags

We calculate time lags between the combined continuum and broad emission-lines flux variations through three methods: the interpolated cross-correlation function (ICCF; Gaskell & Sparke 1986; Gaskell & Peterson 1987), JAVELIN (Zu et al. 2011), and MICA⁶ (Li et al. 2016). For the ICCF method, the time lag is estimated by τ_{cent} , defined as the centroid of the ICCF above 80%

⁶ MICA is available at <https://github.com/LiyAstroph/MICA2>.

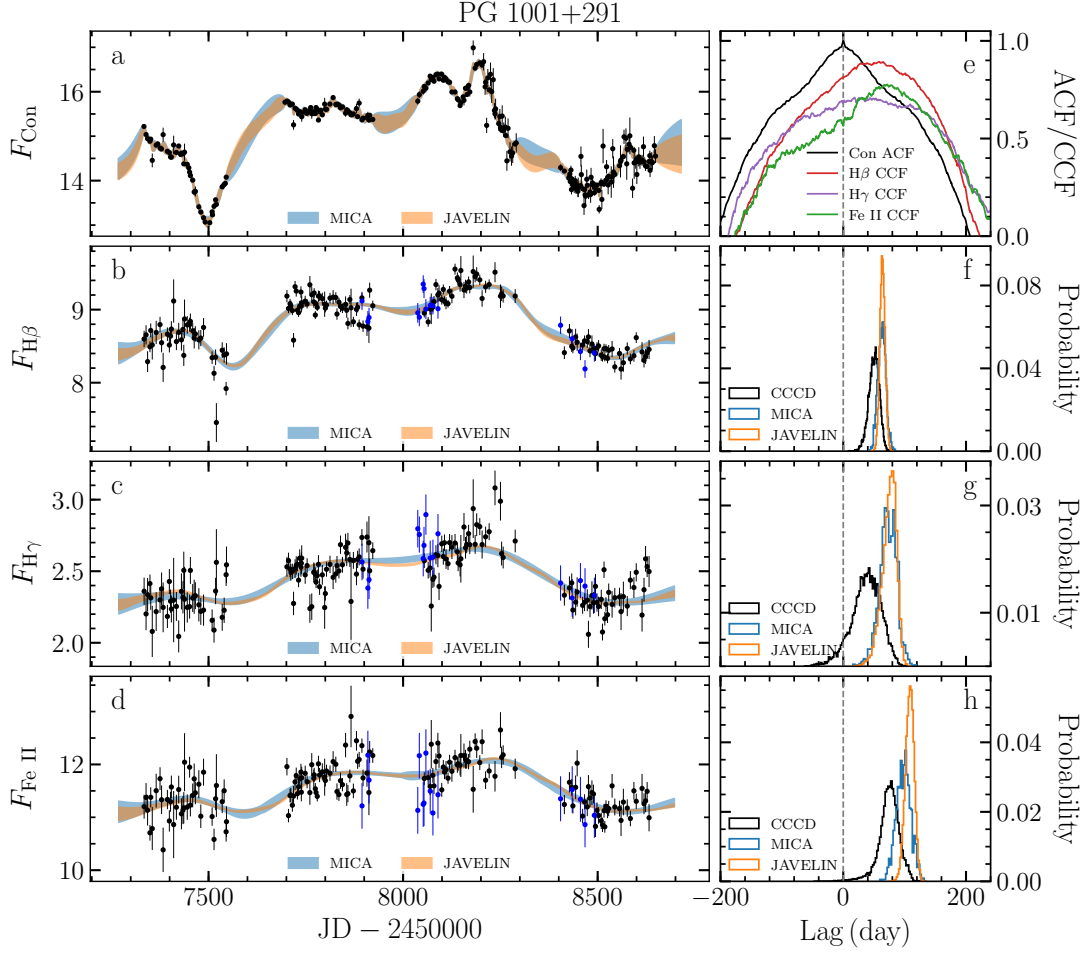


Figure 6. Left panels show the light curves of the combined continuum (a) and broad emission lines (b)-(d). The black and blue points with error bars are from Lijiang and CAHA observations, respectively. Superposed are the reconstructions by JAVELIN (in orange) and MICA (in blue). The units of the continuum and emission line light curves are $10^{-16} \text{ erg s}^{-1} \text{ cm}^{-2} \text{ \AA}^{-1}$ and $10^{-14} \text{ erg s}^{-1} \text{ cm}^{-2}$, respectively. Right panels show time lag analysis. Panel (e) plots the ACF of the combined continuum, and the CCFs between the broad emission lines with continuum light curves. Panels (f)-(h) show the distributions of time delays for the broad emission lines.

Table 4. Light curve statistics

Object	Light Curve	Mean Flux	$F_{\text{var}}(\%)$	R_{max}	τ_{d}	σ_{d}
PG 0923+201	Con	28.06 ± 5.12	17.81 ± 0.59	3.20	965 ± 303	3.47 ± 0.56
	H β	21.78 ± 2.14	9.74 ± 0.75	1.40	315 ± 169	1.88 ± 0.47
	H γ	5.84 ± 0.73	12.06 ± 0.99	1.61	277 ± 167	0.62 ± 0.16
PG 1001+291	Con	14.90 ± 0.90	5.97 ± 0.27	1.30	279 ± 160	0.72 ± 0.19
	H β	8.85 ± 0.37	4.06 ± 0.23	1.28	135 ± 92	0.35 ± 0.10
	H γ	2.46 ± 0.19	6.72 ± 0.48	1.51	158 ± 107	0.15 ± 0.04
	Fe II	11.58 ± 0.44	3.17 ± 0.24	1.24	57 ± 38	0.37 ± 0.08

NOTE—The continuum fluxes are in a unit of $10^{-16} \text{ erg s}^{-1} \text{ cm}^{-2} \text{ \AA}^{-1}$ and the fluxes of all emission lines are in a unit of $10^{-14} \text{ erg s}^{-1} \text{ cm}^{-2}$. Fluxes are corrected with the Galactic extinction. τ_{d} is the rest-frame damping timescale in a unit of day and σ_{d} is the variation amplitude, which has the same unit as the continuum/emission line fluxes (see Section 4.2).

Table 5. Rest-frame time lag and transfer function width measurements

Object	Line	r_{\max}	τ_{cent}	τ_{MICA}	τ_{JAV}	W_{MICA}	W_{JAV}
			(day)			(day)	
PG 0923+201	H β	0.94	$108.2^{+6.6}_{-12.3}$	$105.4^{+4.9}_{-4.9}$	$104.3^{+2.5}_{-1.4}$	$40.2^{+41.6}_{-27.9}$ (45.8 $^{+35.9}_{-33.6}$)	$4.9^{+15.4}_{-4.0}$ (11.6 $^{+8.6}_{-10.8}$)
	H γ	0.90	$121.0^{+8.5}_{-10.2}$	$111.2^{+7.5}_{-6.5}$	$113.9^{+5.3}_{-5.3}$	$21.8^{+19.9}_{-11.7}$ (25.5 $^{+16.1}_{-15.4}$)	$52.5^{+15.7}_{-21.1}$ (50.2 $^{+18.0}_{-18.8}$)
PG 1001+291	H β	0.89	$37.3^{+6.9}_{-6.0}$	$47.5^{+4.7}_{-5.1}$	$48.2^{+3.3}_{-3.1}$	$68.0^{+10.4}_{-9.8}$ (68.3 $^{+10.1}_{-10.1}$)	$89.1^{+8.2}_{-8.0}$ (89.2 $^{+8.1}_{-8.1}$)
	H γ	0.71	$28.0^{+17.9}_{-17.6}$	$55.1^{+10.3}_{-10.3}$	$57.4^{+7.3}_{-10.2}$	$166.9^{+29.2}_{-27.0}$ (168.4 $^{+27.7}_{-28.5}$)	$165.8^{+26.2}_{-34.4}$ (163.0 $^{+29.0}_{-31.6}$)
	Fe II	0.78	$57.2^{+10.5}_{-11.8}$	$74.5^{+8.4}_{-9.3}$	$81.8^{+5.0}_{-5.5}$	$115.7^{+26.6}_{-27.7}$ (114.4 $^{+27.9}_{-26.4}$)	$165.8^{+19.3}_{-21.1}$ (164.9 $^{+20.2}_{-20.2}$)

NOTE—“ W_{MICA} ” is the FWHM of the Gaussian transfer function obtained in the MICA fits, and “ W_{JAV} ” is the width of the top-hat transfer function obtained in the JAVELIN fits. The widths and uncertainties are estimated from the median and 68.3% confidence levels of the corresponding posterior distributions, respectively. The values in brackets refer to the means with the 68.3% confidence levels.

of the peak value (r_{\max} ; Peterson et al. 2004). The uncertainties of time lags are obtained by the 15.87% and 84.13% quantiles of the cross-correlation centroid distributions (CCCDs), generated by the “flux randomization/random subset sampling (FR/RSS)” method (Peterson et al. 1998).

Both JAVELIN and MICA use the damped random walk (DRW) model (e.g, Kelly et al. 2009) to describe the continuum variability and a specific transfer function to fit the light curves of emission lines. JAVELIN adopts a top-hat function to approximate the realistic transfer function, while MICA adopts a family of displaced Gaussians. For simplicity, we use only one Gaussian in MICA. We assign time lags as the centers of the top-hat/ Gaussian. In MICA, we additionally switch on the functionality of including a parameter for any unknown systematic errors, which is added to the data errors in quadrature. JAVELIN employs the affine invariant sampling algorithm (Goodman & Weare 2010; implemented by the package `emcee`⁷) and MICA employs the diffusive nested sampling algorithm (Brewer et al. 2011; implemented by the package `cdnest`⁸) to perform the Markov Chain Monte Carlo (MCMC) technique. This generates posterior samples of the model parameters. The time lags and their associated errors are estimated from the median, 15.87% and 84.13% quantiles of the corresponding posterior distributions. Below, we denote time lags obtained by JAVELIN and MICA as τ_{JAV} and τ_{MICA} , respectively.

In Figures 5 and 6, the left panels show the reconstructed light curves by JAVELIN (in orange) and MICA (in blue). The right panels show the autocorrelation functions (ACFs) of the combined continuum light curves, ICCFs as well as the time lags distributions in the observed frame.

The measured time lags by the three methods are listed in Table 5. We can find general agreements to within uncertainties among the results of the three methods. In particular for PG 0923+201, the time lags of H β and H γ measured from ICCF, JAVELIN and MICA are well consistent with each other. For PG 1001+291, the H β , H γ and Fe II lags obtained by JAVELIN and MICA are in good agreement.

It is worth mentioning that PG 1001+291 was previously monitored by Du et al. (2018b) between 2015 and 2017, who reported an H β time lag of $32.2^{+43.5}_{-4.2}$ days and a mean 5100 Å luminosity of $(3.31 \pm 0.08) \times 10^{45}$ erg s $^{-1}$. The large upper error of the reported H β time lag was caused by the relatively short temporal baseline and low variation amplitudes of the H β light curve. By comparison, our campaign obtains a H β time lag of $37.3^{+6.9}_{-6.0}$ days and a slightly higher mean 5100 Å luminosity of $(3.90 \pm 0.24) \times 10^{45}$ erg s $^{-1}$ (due to variability). The time lag uncertainty of our measurement is more symmetric and significantly reduced.

Figure 7 shows the relationship between time lag ratios of Fe II to H β ($\tau_{\text{Fe II}}/\tau_{\text{H}\beta}$) and flux ratios of Fe II to H β for PG 1001+291 together with the samples of Hu et al. (2015) and 3C 273 from Zhang et al. (2019). The results of PG 1001+291 are generally consistent with the trend that when $\mathcal{R}_{\text{Fe}} > 1$, $\tau_{\text{Fe II}}$ is approximately equal to $\tau_{\text{H}\beta}$, whereas when $\mathcal{R}_{\text{Fe}} < 1$, $\tau_{\text{Fe II}}$ is larger than $\tau_{\text{H}\beta}$.

Through the Monte-Carlo simulation tests described below, we demonstrate that our measured time lags are reliable and not caused by seasonal gaps. We adopt the τ_{cent} values to calculate the black hole masses in the following analysis.

⁷ Available at <https://github.com/dfm/emcee>.

⁸ Available at <https://github.com/LiyiAstroph/CDNest>.

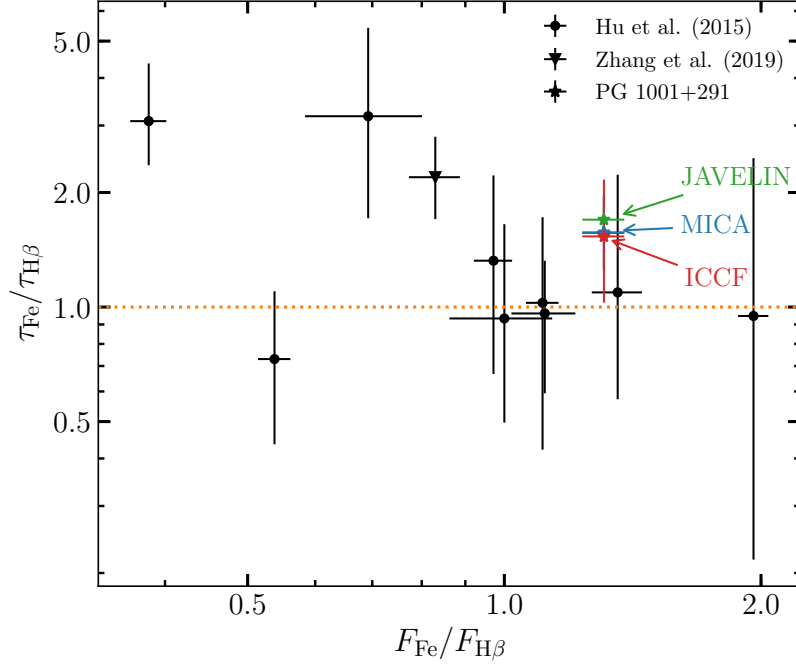


Figure 7. Relation between time lag ratios of Fe II to H β and intensity ratios of Fe II to H β .

4.2. Validity Tests of ICCF Time Lags

Since our light curves have seasonal gaps, we employ Monte-Carlo simulations to test whether the correlations between light curves are caused by seasonal gaps. We generate uncorrelated mock light curves based on the observed light curves of the continuum and broad emission-line. The mock light curves follow the DRW process, which has a covariance between times t_i and t_j (e.g., Kelly et al. 2009)

$$S(t_i, t_j) = \sigma_d^2 \exp\left(-\frac{|t_i - t_j|}{\tau_d}\right), \quad (5)$$

where τ_d is a damping timescale and σ_d is variation amplitude. We first use the observed light curves to determine the parameters τ_d and σ_d and their uncertainties (listed in Table 4), from which we randomly draw pairs of τ_d and σ_d . We then generate two sets of mock light curves with daily samplings and use a linear interpolation onto the observed epochs to mimic real observations. We add Gaussian noises to the mock light curves by enforcing the relative errors equal to these of the observed light curves. We finally use the same ICCF method to calculate r_{\max} of the two sets of light curves. This process is repeated 10000 times and we count the probability that r_{\max} is higher than that of the observed light curves. We call this the false-alarm probability. For PG 0923+201, the false-alarm probabilities of the H β and H γ are 0.0001 and 0.0005, respectively. For PG 1001+291, the false-alarm probabilities of the H β , H γ and Fe II are 0.0007, 0.0260 and 0.0023, respectively. These quantities are relatively low, indicating that the correlations of our light curves are realistic and the influence of seasonal gaps is minor. As an example, we show the r_{\max} distributions of mock light curves for the H β in the left panels of Figure 8.

In addition to the above tests, we also design tests to check whether the obtained time lags are reliable. We use the same method above to construct a daily sampled continuum light curve, and convolve it with a Gaussian transfer function to generate a mock light curve of emission-line. The center and width of the Gaussian transfer function (listed in Table 5) are randomly assigned according to the best estimates and uncertainties obtained by MICA on the observed light curves. The mock light curves are again interpolated onto observed epochs. We repeat this process 10000 times and perform the ICCF method to calculate distributions of τ_{cent} . Figure 8 shows an example of the distributions of H β time lags for mock light curves, which are well consistent with the input values. The results for the other broad lines are similar, implying that our measured time lags are reliable.

4.3. Velocity-resolved Delays

In this section, we calculate velocity-resolved time lags for PG 0923+201 and PG 1001+291, which deliver information about the geometry and kinematics of the BLR.

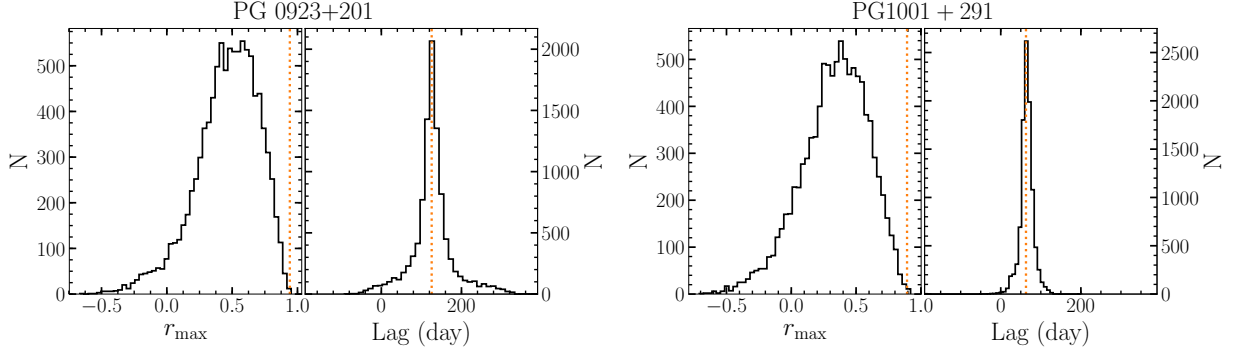


Figure 8. Validity tests of $H\beta$ time lags for PG 0923+201 (top) and PG 1001+291 (bottom). Left panels show r_{\max} distributions of uncorrelated mock light curves from 10000 simulations. The orange dotted lines represent r_{\max} of the observed light curves. Right panels show τ_{cent} distributions of mock light curves. The orange dotted lines represent the input time lags (see Section 4.2 for details).

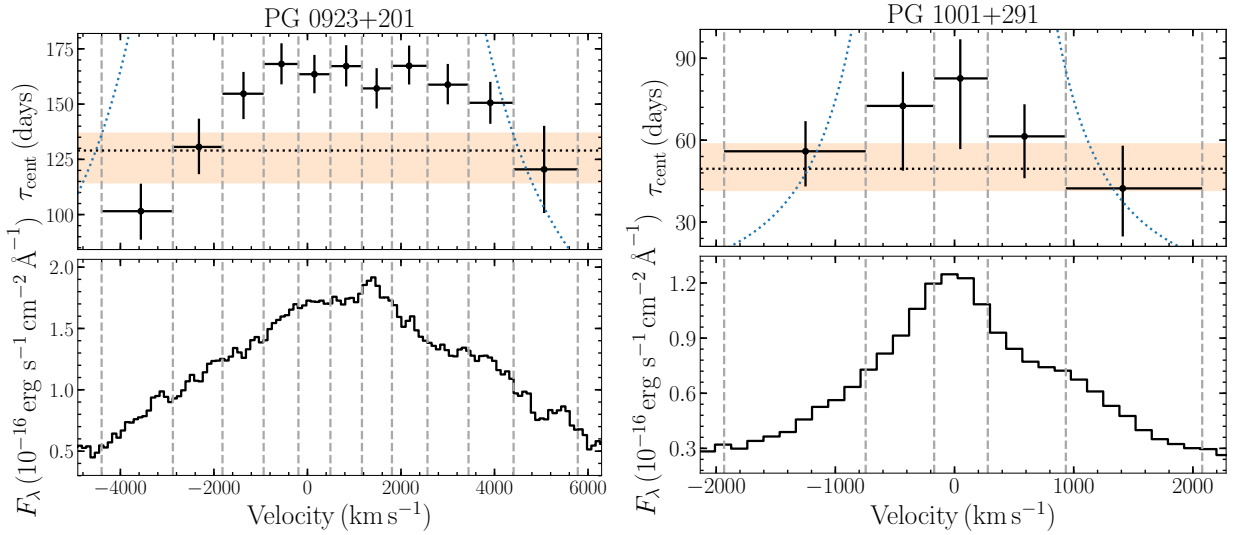


Figure 9. Velocity-resolved lags of the $H\beta$ line in PG 0923+201 (left) and PG 1001+291 (right). The top panels show delays in the observed frame across velocity bins and the bottom panels show the rms spectra of the broad $H\beta$. The vertical dashed lines show the boundaries of velocity bins. The delay in each bin is calculated by the ICCF method. The horizontal dotted lines and orange band show the mean $H\beta$ centroid lag and the associated uncertainties measured in Section 4.1. The blue dotted curves show the virial envelopes for a Keplerian disk with an inclination of $\cos i = 0.75$ and the estimated black hole mass in Table 6.

Table 6. $H\beta$ line width measurements and black hole mass estimates

Object	Mean Spectrum		rms Spectrum		M_{\bullet}	L_{5100}	\mathcal{M}
	FWHM	σ_{line}	FWHM	σ_{line}			
	(km s ⁻¹)		(km s ⁻¹)		(10 ⁷ M_{\odot})	(10 ⁴⁵ erg s ⁻¹)	
PG 0923+201	7469 ± 273	3156 ± 109	6853 ± 214	2914 ± 88	118 ⁺¹¹ ₋₁₆	2.05 ± 0.29	0.21 ^{+0.06} _{-0.07}
PG 1001+291	2138 ± 9	1320 ± 4	2108 ± 120	896 ± 51	3.33 ^{+0.62} _{-0.54}	3.90 ± 0.24	679 ⁺²⁵⁹ ₋₂₂₇

With the spectral decompositions, we extract the broad $H\beta$ component of the model fitted to each individual spectrum and calculate the rms spectrum. We then divide the rms spectrum into several velocity bins, each bin with the same integrated flux. The light curve of each bin is cross-correlated against the combined continuum to obtain time lags. The results are shown in

Figure 9, where the top panels show the velocity-resolved delays and the bottom panels show the rms spectra of the broad H β . In Appendix, we also show the light curves and ICCF analysis of each velocity bin. Below we comment on each object individually.

PG 0923+201—The result shows shorter lags at higher velocities on both red and blue wings of the line profile, as would be expected for virialized motions. However, the lags in the redshifted bins are overall longer than these in the blueshifted bins, which might indicate a signature of outflow (Bentz et al. 2009; Du et al. 2018a). The virial envelopes in Figure 9 clearly show the asymmetric lag structure. We note that the center wavelengths of the narrow lines in our spectra (see Figure 3) are correct, meaning that this asymmetry is real. A similar pattern can be seen in other objects, such as NGC 3227 (Denney et al. 2009) and Mrk 79 (Lu et al. 2019). This complicated structure may imply the coexistence of virialization and outflow in the BLR of PG 0923+201.

PG 1001+291—The lag structure of PG 1001+291 is relatively symmetric and also shows smaller delays in both wings of the line profile, basically agreeing with the virial envelopes. However, this object has a low variability in each velocity bin of the H β line, resulting in broad ICCFs and large lag errors. Further spectroscopic monitoring on PG 1001+291 is warranted to strengthen the evidence on the velocity-delay structure.

We also use the Monte-Carlo simulation method described in Section 4.2 to calculate the false-alarm probability (in terms of r_{\max}) for each wavelength bin in the delay maps. The resulting false-alarm probabilities range between 0.0001 and 0.0197 for PG 0923+201, and between 0.0022 and 0.0116 for PG 1001+291. Again, these quantities are relatively low, indicating that the correlations over wavelength bins are not dominated by seasonal gaps.

4.4. Black Hole Masses and Accretion Rates

We use Equation (1) to calculate the black hole mass. There are two line width measures, namely, FWHM and line dispersion (σ_{line}) of mean or rms spectra. To measure H β widths from the mean spectrum, we need to subtract the narrow line components. We assume that the narrow H β has the same profile and a fixed flux ratio of 0.1 to the [O III] λ 5007. Regarding uncertainties of the line width, we consider the following factors. First, the contribution from the narrow line is estimated by setting a flux ratio of 0 and 0.2 between the narrow H β to [O III] λ 5007. As such, we derive an upper and lower line width and assign the uncertainty as the average of the differences to the fiducial value with a flux ratio of 0.1. Second, we use the bootstrap method to estimate the uncertainties of line widths caused by data sampling (see, e.g., Peterson et al. 2004). Specifically, we randomly select N spectra (with replacement) from our N total spectra and remove duplicate spectra in creating a new mean spectrum. We apply the above procedure to this newly generated mean spectrum to calculate its FWHM and σ_{line} . We repeat this process 1000 times to obtain line width distributions, from which we determine the standard deviations and assign them as the uncertainties. Finally, for PG 0923+201, we additionally include the influence of the He II by assigning the contributed uncertainty as the difference between the line widths with and without adding a He II component in the spectral decomposition. We combine the above uncertainties in quadrature to get the final line width uncertainties.

For the rms spectrum, we determine line widths by spectral fitting, as shown in the bottom panels of Figure 3. The fitting components for the rms spectrum in PG 0923+201 include: (1) a single power law, (2) a single Gaussian for H β , He II, H γ ; and in PG 1001+291 include: (1) a single power law, (2) an Fe II template from Boroson & Green (1992), (3) a single Gaussian for H β and H γ . The corresponding uncertainties are determined by the same bootstrap method as applied for the mean spectrum described above.

From all measured line widths we subtract in quadrature the instrumental broadening (Section 2.2) to obtain the results in Table 6. Following Du et al. (2018b), we adopt τ_{cent} and the H β FWHM from the mean spectrum and $f_{\text{BLR}} = 1$ to measure the black hole mass. The mass errors simply include the uncertainties of time lags and line widths. We obtain a black hole mass of $118_{-16}^{+11} \times 10^7 M_{\odot}$ for PG 0923+201 and $3.33_{-0.54}^{+0.62} \times 10^7 M_{\odot}$ for PG 1001+291.

We also measure the black hole mass using the broad H γ line. Because the velocity width and shift of H γ are fixed to those of H β in fitting the mean spectrum, we resort to the FWHM from the rms spectrum. For PG 0923+201 and PG 1001+291, the FWHMs of H γ are 7572 ± 404 and 1884 ± 250 km s $^{-1}$, respectively. Again, using the width and τ_{cent} of H γ and $f_{\text{BLR}} = 1$, we estimate the black hole mass to be $135_{-18}^{+17} \times 10^7 M_{\odot}$ for PG 0923+201 and $1.94_{-1.32}^{+1.34} \times 10^7 M_{\odot}$ for PG 1001+291 respectively. The obtained black hole masses from the H β and H γ are consistent with each other.

According to the standard accretion disk model (Shakura & Sunyaev 1973), the dimensionless accretion rate (Eddington ratio) defined as $\dot{\mathcal{M}} = \dot{M}_{\bullet} c^2 / L_{\text{Edd}}$ can be estimated by (Du et al. 2016b)

$$\dot{\mathcal{M}} = 20.1 \left(\frac{\ell_{44}}{\cos i} \right)^{3/2} m_7^{-2}, \quad (6)$$

where \dot{M}_\bullet is the accretion rate, L_{Edd} is the Eddington luminosity, $\ell_{44} = L_{5100}/10^{44}\text{erg s}^{-1}$, $m_7 = M_\bullet/10^7 M_\odot$, and i is the inclination angle of the accretion disk. We take $\cos i = 0.75$, which represents a mean disk inclination for a type 1 AGN by assuming that the inclination randomly distributes between 0 and 60 degrees. We estimate the flux contributions from the host galaxies based on the empirical relation proposed by Shen et al. (2011), which is written as $L_{5100,\text{host}}/L_{5100,\text{AGN}} = 0.8052 - 1.5502x + 0.912x^2 - 0.1577x^3$, for $x < 1.053$, where $L_{5100,\text{host}}$ and $L_{5100,\text{AGN}}$ are the luminosity of host and AGN at 5100 Å respectively, $x = \log(L_{5100,\text{tot}}/10^{44}\text{erg s}^{-1})$, and $L_{5100,\text{tot}}$ is the total luminosity at 5100 Å. For $x > 1.053$, the luminosity correction is unnecessary. For PG 0923+201 and PG 1001+291, $x = 1.380$ and 1.623 , respectively, meaning that the contribution of host galaxies can be neglected. This also demonstrates that it is reasonable to omit the host galaxy component in our spectral decompositions in Section 3.1. We calculate the mean flux of the continuum light curve obtained by the spectral fitting and use it to compute the luminosity at 5100 Å. Combining the \dot{M}_\bullet and L_{5100} , we estimate \mathcal{M} to be $0.21_{-0.07}^{+0.06}$ for PG 0923+201 and 679_{-227}^{+259} for PG 1001+291. This implies that PG 0923+201 is a sub-Eddington accretor whereas PG 1001+291 is a super-Eddington accretor.

In the above calculations, we adopt a virial factor of $f_{\text{BLR}} = 1$. Since the two objects have significantly different properties, their virial factors might be different. Several previous studies proposed that the virial factor f_{BLR} for H β line is anticorrelated with the FWHM (e.g., Mejía-Restrepo et al. 2018; Yu et al. 2019; Martínez-Aldama et al. 2019). Using the relation of Mejía-Restrepo et al. (2018)

$$f_{\text{BLR}}^c = \left(\frac{\text{FWHM}}{4550 \pm 1000} \right)^{-1.17}, \quad (7)$$

we obtain the virial factor based on the FWHM from the mean spectrum 0.56 ± 0.14 for PG 0923+201, and 2.42 ± 0.62 for PG 1001+291. With this new virial factor, the black hole masses are estimated to be $66_{-19}^{+18} \times 10^7 M_\odot$ for PG 0923+201 and $8.05_{-2.44}^{+2.55} \times 10^7 M_\odot$ for PG 1001+291. Correspondingly, the dimensionless accretion rates are changed to $0.66_{-0.40}^{+0.38}$ and 116_{-71}^{+74} , respectively. This still indicates that PG 0923+201 is a sub-Eddington accretor and PG 1001+291 is a super-Eddington accretor, retaining the conclusion with $f_{\text{BLR}} = 1$.

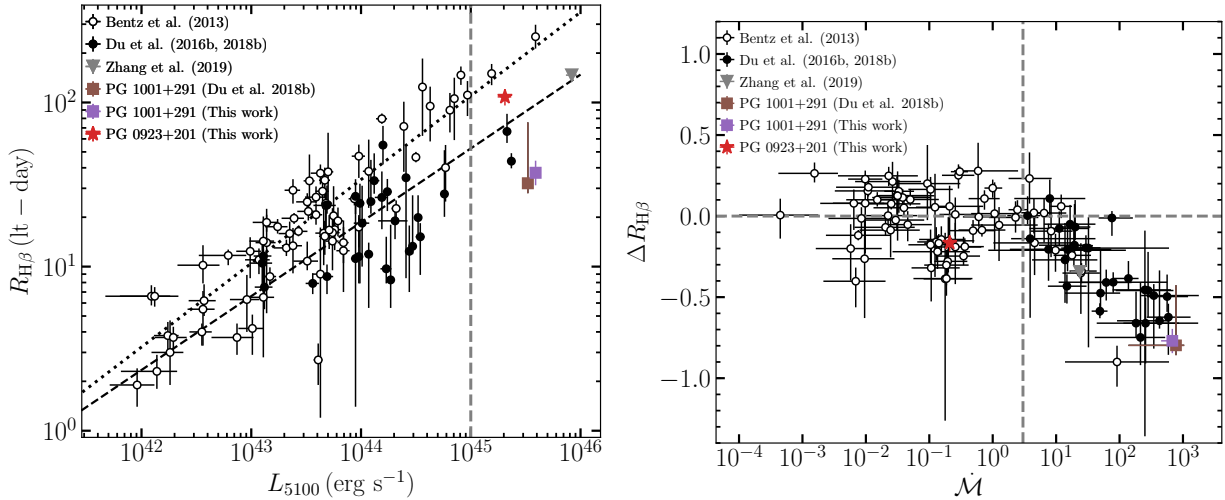


Figure 10. (Left) the $R_{\text{H}\beta} - L_{5100}$ relation. The dotted and dashed lines are the best fit to the AGNs with $\mathcal{M} < 3$ and with $\mathcal{M} \geq 3$ from Du et al. (2018b). The RM objects with luminosities above $10^{45} \text{erg s}^{-1}$ are located to the right of the vertical dashed line. (Right) the relation between $\Delta R_{\text{H}\beta}$ and \mathcal{M} . The vertical and horizontal dashed lines indicate $\mathcal{M} = 3$ and $\Delta R_{\text{H}\beta} = 0$, respectively (see Section 5.1 for the definition of $\Delta R_{\text{H}\beta}$).

5. DISCUSSION

5.1. Implication for $R_{\text{H}\beta} - L_{5100}$ Relation

In the left panel of Figure 10, we plot the H β lag and L_{5100} of PG 0923+201 and PG 1001+291 along with the previous compiled sample of Bentz et al. (2013) and samples from the SEAMBH campaigns (Du et al. 2015, 2016b, 2018b). There are seven RM AGNs with luminosities above $10^{45} \text{erg s}^{-1}$ to date. For comparison, we also superimpose the empirical $R_{\text{H}\beta} - L_{5100}$ relation from Du et al. (2018b). The dotted line represents the relation for RM sample with $\mathcal{M} < 3$, which is consistent with Bentz

et al. (2013)’s compilation. The dashed line represents the relation for RM sample with $\dot{\mathcal{M}} \geq 3$. The location of PG 1001+291 is almost unchanged compared to the previous measurement of Du et al. (2018b). The H β time delay of PG 0923+201 is consistent with the empirical $R_{\text{H}\beta} - L_{5100}$ relations of both Bentz et al. (2013) and Du et al. (2018b), in consideration of their associated scatters. However, PG 1001+291 lies 0.78 dex below the empirical $R_{\text{H}\beta} - L_{5100}$ relation of Bentz et al. (2013). The reported scatter σ of the Bentz et al. (2013) relation is about 0.19 and the deviation of PG 1001+291 exceeds a 4σ significance. This deviation is believed to be caused by the physical dependence of the $R_{\text{H}\beta} - L_{5100}$ relation on the dimensionless accretion rates. According to the results of Du et al. (2015, 2016b, 2018b), there is a strong correlation between time lag shortening in SEAMBHs and accretion rates. A possible explanation for time lag shortening was proposed by Wang et al. (2014b). Specifically, slim accretion disks with super-Eddington accretion rates produce strong self-shadowing effects, resulting in a strongly anisotropic radiation field and two dynamically distinct BLR regions with different delays (Wang et al. 2014b). The BLR is thereby divided into a shadowed region and an unshadowed region (Du et al. 2018b). Since the shadowed region receives fewer ionizing photons, its size shrinks, leading to a shortened time delay. Another possible explanation was that the time lag shortening is caused by the changes of the UV/optical spectral energy distribution and the relative amount of ionizing radiation, which may be related to the black hole spin and accretion rate (e.g., Wang et al. 2014a; Czerny et al. 2019; Fonseca Alvarez et al. 2020).

According to the $R_{\text{H}\beta} - L_{5100}$ relation of Du et al. (2018b),

$$\log\left(\frac{R_{\text{H}\beta}}{\text{lt d}}\right) = \begin{cases} (1.53 \pm 0.03) + (0.51 \pm 0.03) \log \ell_{44}, & (\dot{\mathcal{M}} < 3) \\ (1.26 \pm 0.04) + (0.45 \pm 0.05) \log \ell_{44}, & (\dot{\mathcal{M}} \geq 3) \end{cases} \quad (8)$$

we can find that PG 0923+201 and PG 1001+291 are located within 2σ of the relation with $\dot{\mathcal{M}} < 3$ and 3σ of the relation with $\dot{\mathcal{M}} \geq 3$, respectively. This confirms that the $R_{\text{H}\beta} - L_{5100}$ relation at the high-luminosity end still strongly depends on the dimensionless accretion rates. Following Du et al. (2015), we define $\Delta R_{\text{H}\beta} = \log(R_{\text{H}\beta}/R_{\text{H}\beta, \text{R-L}})$ to measure the deviation from the $R_{\text{H}\beta} - L_{5100}$ relation for $\dot{\mathcal{M}} < 3$ and plot $\Delta R_{\text{H}\beta}$ as a function of the dimensionless accretion rate $\dot{\mathcal{M}}$ in the right panel of Figure 10. PG 1001+291 clearly deviates from the canonical relation by about 0.8 dex. Figure 10 demonstrates that H β time lags are more severely shortened for higher accretion rates. Therefore, it is important to take accretion rates into account when estimating the black hole mass of luminous AGNs at super-Eddington accretion rates.

5.2. Locations in the Eigenvector 1 Plane of RM Samples

In Figure 11, we plot the distribution of RM samples in the Eigenvector 1 (EV1) plane (also known as the main sequence) by including the compilation of Du & Wang (2019) and two objects obtained in this work. Here, the EV1 plane refers to the \mathcal{R}_{Fe} versus $\text{FWHM}_{\text{H}\beta}$ (FWHM of the broad H β) plane. Sulentic et al. (2000) divides AGNs into populations A and B according to the value of $\text{FWHM}_{\text{H}\beta}$, where AGNs with $\text{FWHM}_{\text{H}\beta} \leq 4000 \text{ km s}^{-1}$ are classified as Population A, otherwise as Population B. Population A includes NLS1s and high accretors (Marziani & Sulentic 2014), while Population B has larger black hole masses and lower accretion rates (Sulentic et al. 2011). It is generally believed that the accretion rate and Eddington ratio increase with \mathcal{R}_{Fe} , and the dispersion of $\text{FWHM}_{\text{H}\beta}$ for a given \mathcal{R}_{Fe} characterizes the orientation effect (Marziani et al. 2001; Shen & Ho 2014). PG 1001+291 is located in the region of high \mathcal{R}_{Fe} and narrow $\text{FWHM}_{\text{H}\beta}$, consistent with our results that PG 1001+291 is accreting at a super-Eddington rate. We note that the \mathcal{R}_{Fe} of PG 1001+291 is larger than the previous measurement of Du & Wang (2019) due to variability.

We simply follow Sulentic et al. (2011) to define outliers in the Eigenvector 1 plane, namely, those AGNs with $\text{FWHM}_{\text{H}\beta} > 4000 \text{ km s}^{-1}$ and $\mathcal{R}_{\text{Fe}} > 0.5$. PG 0923+201 is the most significant outlier in the present RM sample. The reasons for such an ‘‘outlier’’ location of PG 0923+201 in the EV1 plane are not yet clear. However, we note that this definition of ‘‘outlier’’ is only phenomenological. Meanwhile, we cannot exclude the possibility that the significant deviation might be caused by real differences between PG 0923+201 and the RM sample of Du & Wang (2019). The majority of the Du & Wang (2019) sample have low luminosities and black hole masses and therefore the corresponding FWHMs are generally small. Nevertheless, from the large SDSS quasar sample, there also exists a population of AGNs that have relatively large \mathcal{R}_{Fe} and broad H β line widths like PG 0923+201 (see Shen & Ho 2014). Detailed multiwavelength investigations of these quasars might help reveal additional BLR and SMBH accretion physics.

6. CONCLUSION

We present a reverberation mapping campaign of two luminous quasars at the high-luminosity end of the $R_{\text{H}\beta} - L_{5100}$ relation. Our main results are as follows.

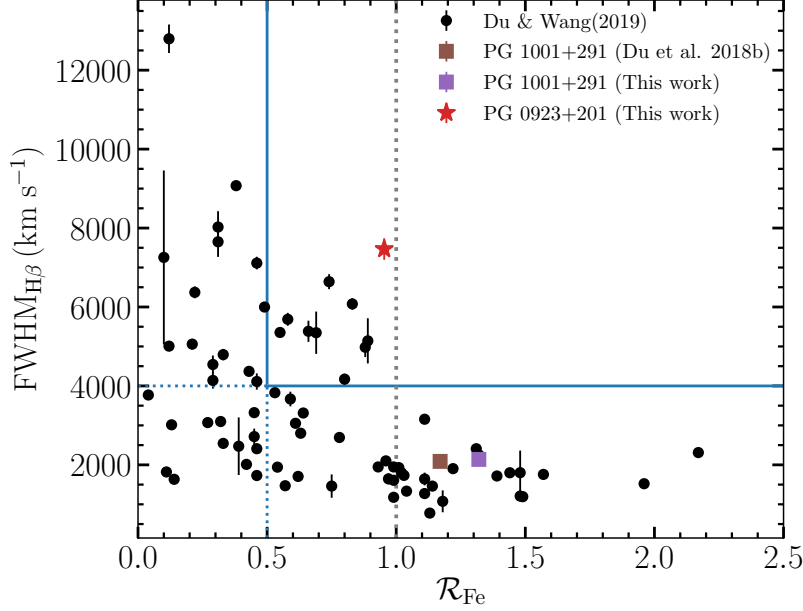


Figure 11. The main sequence of RM samples. The black points were compiled by Du & Wang (2019). The blue horizontal and vertical lines corresponds to $\text{FWHM}_{\text{H}\beta} = 4000 \text{ km s}^{-1}$ and $\mathcal{R}_{\text{Fe}} = 0.5$, respectively, and the gray dotted line represent $\mathcal{R}_{\text{Fe}} = 1.0$. The upper right corner enclosed by the blue solid lines is defined as the “outlier” region according to Sulentic et al. (2011).

- We measure the time delays of the broad emission lines with respect to the 5100 \AA continuum. Using the ICCF method, the $\text{H}\beta$ and $\text{H}\gamma$ lags of PG 0923+201 in the rest frame are $108.2^{+6.6}_{-12.3}$ and $121.0^{+8.5}_{-10.2}$ days, respectively, and the $\text{H}\beta$, $\text{H}\gamma$, Fe II lags of PG 1001+291 are $37.3^{+6.9}_{-6.0}$, $28.0^{+17.9}_{-17.6}$ and $57.2^{+10.5}_{-11.8}$ days, respectively.
- The velocity-resolved delays of the $\text{H}\beta$ line in PG 0923+201 show a virialized motion, with shorter lags at line wings and longer lags at line core. However, the lags in the redshifted bins are higher than those in the blueshifted bins. This complicated structure may indicate the coexistence of virialized motion and outflow in the BLR of PG 0923+201. The lag structure of PG 1001+291 is relatively symmetric and also shows a virialized BLR.
- Based on the $\text{H}\beta$ delays and FWHMs in the mean spectra, and assuming a virial factor of $f_{\text{BLR}} = 1$, we estimate the black hole masses to be $118^{+11}_{-16} \times 10^7 M_{\odot}$ for PG 0923+201 and $3.33^{+0.62}_{-0.54} \times 10^7 M_{\odot}$ for PG 1001+291. We obtain consistent mass estimates using the $\text{H}\gamma$ line. The accretion rates of PG 0923+201 and PG 1001+291 are estimated to be $0.21^{+0.06}_{-0.07} L_{\text{Edd}} c^{-2}$ and $679^{+259}_{-227} L_{\text{Edd}} c^{-2}$, respectively, indicating that PG 0923+201 is accreting at a sub-Eddington rate whereas PG 1001+291 is a super-Eddington accretor.
- The $\text{H}\beta$ time lag of PG 1001+291 falls 0.78 dex below the empirical $R_{\text{H}\beta} - L_{5100}$ relation of Bentz et al. (2013), confirming that even for high-luminosity quasars, $\text{H}\beta$ time lags depend on both luminosity and Eddington ratio, as previously found by Du et al. (2018b). This strengthens the conclusion that the $R_{\text{H}\beta} - L_{5100}$ relation at the high-luminosity end needs to consider the influences of accretion rates. The uncomfortably high single-epoch black hole masses estimated for AGN at large redshifts may be significantly over-estimated if this effect has not been taken into account.

We thank the referee for useful comments that improved the manuscript. This work is supported by the National Key R&D Program of China (2016YFA0400701, 2016YFA0400702), by the National Science Foundation of China (NSFC-11721303, 11773029, 11833008, 11873048, 11922304, 11973029, 11991051, 11991052, 11991053, 11991054, 12003036, 12022301), by the Key Research Program of Frontier Sciences of the Chinese Academy of Sciences (CAS; YZDJ-SSW-SLH007), by the CAS Key Research Program (KJZDEW-M06), by the CAS International Partnership Program (113111KYSB20200014), and by the Strategic Priority Research Program of the CAS (XDB23000000, XDB23010400). We acknowledge the support of the staff of the Lijiang 2.4 m telescope. Funding for the telescope has been provided by the CAS and the People’s Government of Yunnan Province. We also acknowledge the support of the staff of the CAHA 2.2 m telescope. Y.-R.L. acknowledges financial support from the Youth Innovation Promotion Association CAS. K.H. acknowledges support from STFC grant ST/R000824/1. Based on

observations obtained with the Samuel Oschin Telescope 48-inch and the 60-inch Telescope at the Palomar Observatory as part of the Zwicky Transient Facility project. ZTF is supported by the National Science Foundation and a collaboration including Caltech, IPAC, the Weizmann Institute for Science, the Oskar Klein Center at Stockholm University, the University of Maryland, Deutsches Elektronen-Synchrotron and Humboldt University, Lawrence Livermore National Laboratory, the TANGO Consortium of Taiwan, the University of Wisconsin at Milwaukee, Trinity College Dublin, and Institut national de physique nucléaire et de physique des particules. Operations are conducted by COO, IPAC and University of Washington. This research has made use of the NASA/IPAC Extragalactic Database (NED) which is operated by the Jet Propulsion Laboratory, California Institute of Technology, under contract with the National Aeronautics and Space Administration.

Software: DASpec (<https://github.com/PuDu-Astro/DASpec>), PyCALI (Li et al. 2014), MICA (Li et al. 2016), JAVELIN (Zu et al. 2011).

APPENDIX

A. SPECTRAL DECOMPOSITIONS WITH INCLUDING THE He II COMPONENT

In this appendix, we present the fitting results of PG 0923+201 by adding a He II component. The SFS is similar to that described in Section 3.1 except for adding a Gaussian to account for the He II line (see Figure 12). In each individual spectrum, the He II is too weak and highly blended with the Fe II. Therefore, to reduce the degeneracy, the line width and shift of the He II are fixed to the best values obtained by fitting the rms spectrum (in the bottom panel of Figure 3). The measured light curves and time lag analysis are shown in Figure 13. The obtained time delays are summarized in Table 7.

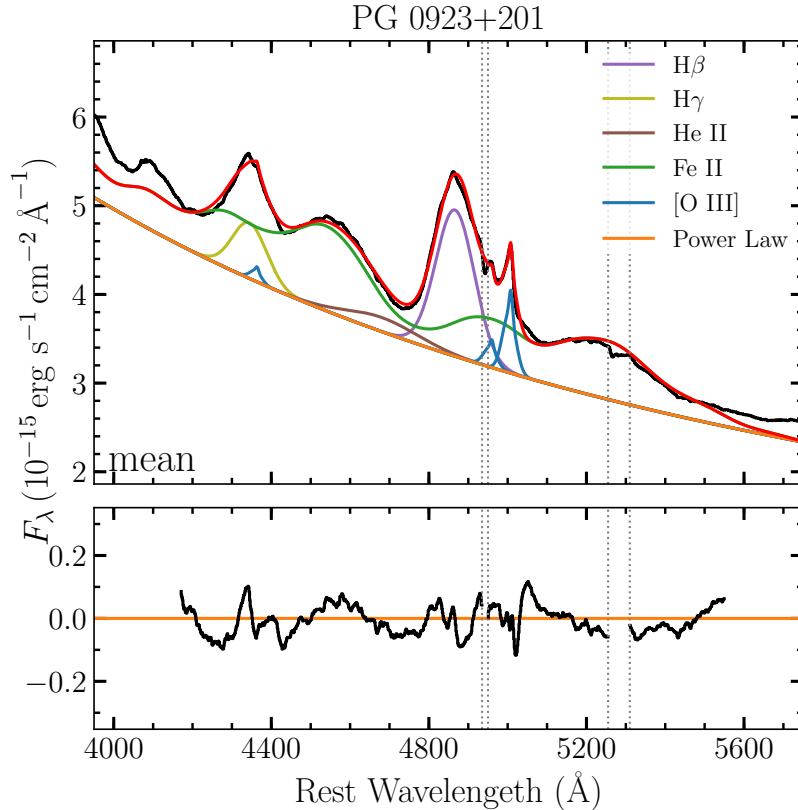
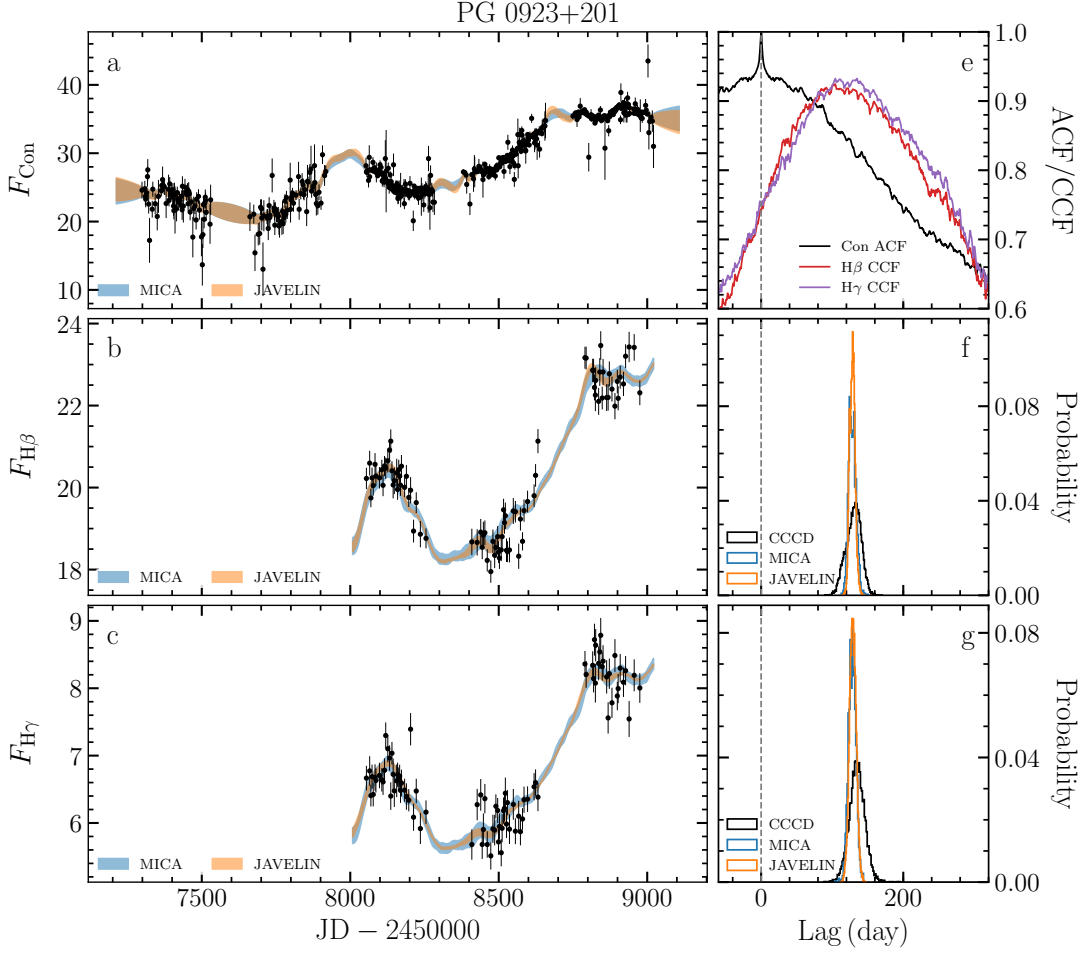


Figure 12. A spectral decomposition of the mean spectrum for PG 0923+201 with including a He II $\lambda 4686$ component. The top and bottom panels show the details of the spectral decomposition and the residuals in the fitting window, respectively. The vertical dotted lines indicate the regions omitted from the fit.

B. ICCF RESULTS IN EACH VELOCITY BIN

Table 7. Rest-frame time lag measurements by including a He II component in spectral decompositions

Object	Line	τ_{\max}	τ_{cent}	τ_{MICA}	τ_{JAV}
			(day)		
PG 0923+201	H β	0.92	$110.1^{+7.7}_{-10.5}$	$107.4^{+4.5}_{-3.9}$	$107.8^{+3.0}_{-3.4}$
	H γ	0.93	$111.9^{+10.2}_{-7.6}$	$107.6^{+4.3}_{-4.4}$	$108.3^{+3.9}_{-3.8}$


Figure 13. Same as Figure 5, but for spectral decompositions including a He II component.

In Figure 14, we show the H β light curves, ICCFs and CCCDs at different velocity bins for PG 0923+201 and PG 1001+291.

REFERENCES

- Bahcall, J. N., Kozlovsky, B.-Z., & Salpeter, E. E. 1972, *ApJ*, 171, 467
- Barth, A. J., Pancoast, A., Bennert, V. N., et al. 2013, *ApJ*, 769, 128
- Barth, A. J., Pancoast, A., Thorman, S. J., et al. 2011, *ApJL*, 743, L4
- Barth, A. J., Bennert, V. N., Canalizo, G., et al. 2015, *ApJS*, 217, 26

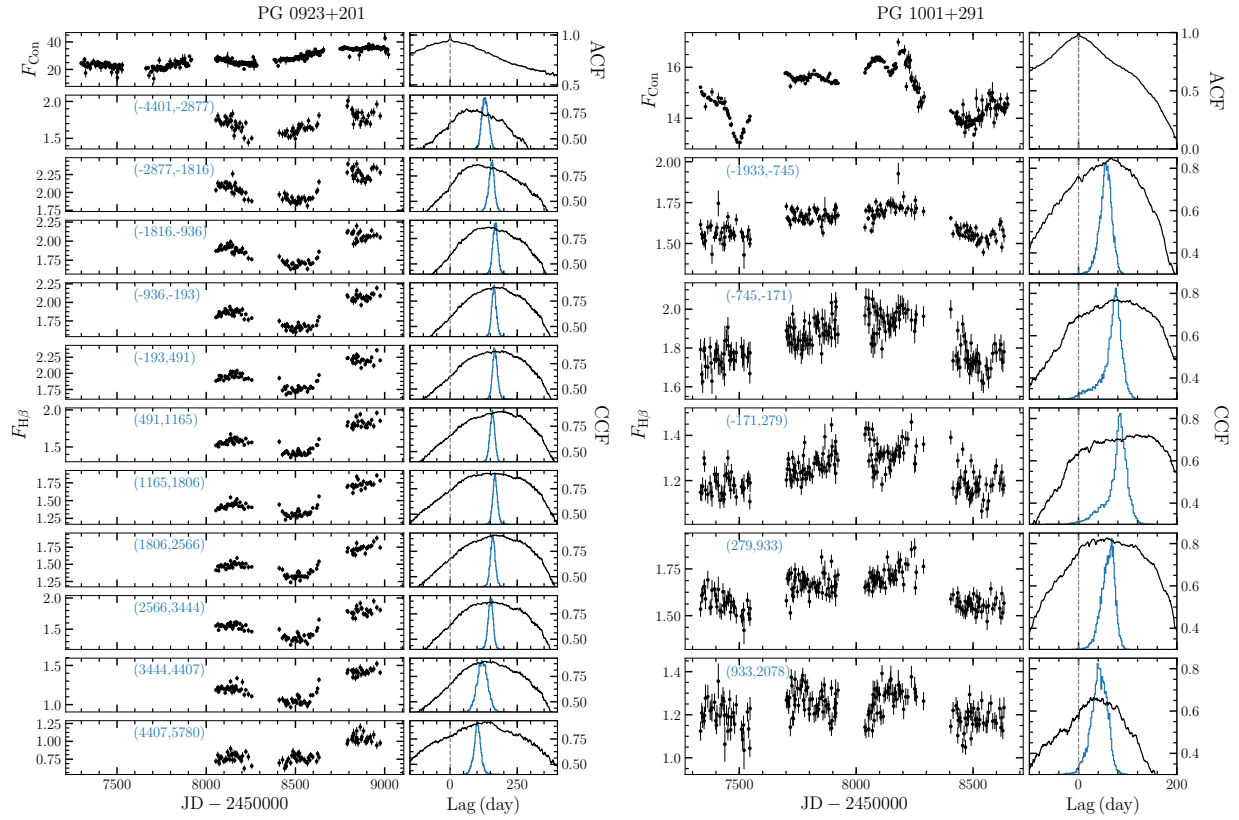


Figure 14. The topmost panels show the continuum light curves and ACFs. The rest panels show the H β light curves (black points with error bars), ICCFs (black lines) and CCCDs (blue histograms) at each velocity bin for (left) PG 0923+201 and (right) PG 1001+291. The units of the continuum and H β light curves are 10^{-16} erg s $^{-1}$ cm $^{-2}$ Å $^{-1}$ and 10^{-14} erg s $^{-1}$ cm $^{-2}$, respectively. The velocity bin edges are marked by pairs of numbers (in units of km s $^{-1}$).

Bellm, E. C., Kulkarni, S. R., Graham, M. J., et al. 2019, *PASP*, 131, 018002

Bentz, M. C., Denney, K. D., Grier, C. J., et al. 2013, *ApJ*, 767, 149

Bentz, M. C., Walsh, J. L., Barth, A. J., et al. 2008, *ApJL*, 68

Bentz, M. C., Walsh, J. L., Barth, A. J., et al. 2009, *ApJ*, 705, 199

Bentz, M. C., Walsh, J. L., Barth, A. J., et al. 2010, *ApJ*, 716, 993

Blandford, R. D., & McKee, C. F. 1982, *ApJ*, 255, 419

Borison, T. A., & Green, R. F. 1992, *ApJS*, 80, 109

Brewer, B. J., Páatay, L. B., & Csányi, G. 2011, *Stat. Comput.*, 21, 649

Cardelli, J. A., Clayton, G. C., & Mathis, J. S. 1989, *ApJ*, 345, 245

Czerny, B., Wang, J.-M., Du, P., et al. 2019, *ApJ*, 870, 84

De Rosa, G., Fausnaugh, M. M., Grier, C. J., et al. 2018, *ApJ*, 866, 133

Denney, K. D., Peterson, B. M., Pogge, R. W., et al. 2009, *ApJL*, 704, L80

Denney, K. D., Peterson, B. M., Pogge, R. W., et al. 2010, *ApJ*, 721, 715

Du, P., Hu, C., Lu, K.-X., et al. 2014, *ApJ*, 782, 45

Du, P., Hu, C., Lu, K.-X., et al. 2015, *ApJ*, 806, 22

Du, P., Lu, K.-X., Hu, C., et al. 2016a, *ApJ*, 820, 27

Du, P., Lu, K.-X., Zhang, Z.-X., et al. 2016b, *ApJ*, 825, 126

Du, P., Brotherton, M. S., Wang, K., et al. 2018a, *ApJ*, 869, 142

Du, P. & Wang, J.-M. 2019, *ApJ*, 886, 42

Du, P., Zhang, Z.-X., Wang, K., et al. 2018b, *ApJ*, 856, 6

Edelson, R., Gelbord, J., Cackett, E., et al. 2019, *ApJ*, 870, 123

Edelson, R., Turner, T. J., Pounds, K. et al. 2002, *ApJ*, 568, 610

Fausnaugh, M. M., Grier, C. J., Bentz, M. C., et al. 2017, *ApJ*, 840, 97

Feng, H.-C., Hu, C., Li, S.-S., et al. 2021, *ApJ*, 909, 18

Fonseca Alvarez, G., Trump, J. R., Homayouni, Y., et al. 2020, *ApJ*, 899, 73

Gaskell, C. M., & Peterson, B. M. 1987, *ApJS*, 65, 1

Gaskell, C. M. & Sparke, L. S. 1986, *ApJ*, 305, 175

Giveon, U., Maoz, D., Kaspi, S., et al. 1999, *MNRAS*, 306, 637

Goodman, J. & Weare, J. 2010, *Communications in Applied Mathematics and Computational Science*, 5, 65

Graham, M. J., Kulkarni, S. R., Bellm, E. C., et al. 2019, *PASP*, 131, 078001

Grier, C. J., Peterson, B. M., Pogge, R. W., et al. 2012, *ApJ*, 755, 60

Grier, C. J., Trump, J. R., Shen, Y., et al. 2017, *ApJ*, 851, 21

Henden, A. A., Levine, S. E., Terrell, D., et al. 2012, *Journal of the American Association of Variable Star Observers (JAAVSO)*, 40, 430

- Ho, L. C. & Kim, M. 2014, *ApJ*, 789, 17
- Hook, I. M., McMahon, R. G., Boyle, B. J., et al. 1994, *MNRAS*, 268, 305
- Hu, C., Du, P., Lu, K.-X., et al. 2015, *ApJ*, 804, 138
- Hu, C., Li, S.-S., Guo, W.-J., et al. 2020a, *ApJ*, 905, 75
- Hu, C., Li, S.-S., Yang, S., et al. 2021, *ApJS*, 253, 20
- Hu, C., Li, Y.-R., Du, P., et al. 2020b, *ApJ*, 890, 71
- Huang, Y.-K., Hu, C., Zhao, Y.-L., et al. 2019, *ApJ*, 876, 102
- Kaspi, S., Smith, P. S., Netzer, H., et al. 2000, *ApJ*, 533, 631
- Kelly, B. C., Bechtold, J., & Siemiginowska, A. 2009, *ApJ*, 698, 895
- Kochanek, C. S., Shappee, B. J., Stanek, K. Z., et al. 2017, *PASP*, 129, 104502
- Kollatschny, W., Ulbrich, K., Zetzl, M., et al. 2014, *A&A*, 566, A106
- Li, Y.-R., Wang, J.-M., & Bai, J.-M. 2016, *ApJ*, 831, 206
- Li, Y.-R., Wang, J.-M., Hu, C., et al. 2014, *ApJL*, 786, L6
- Lu, K.-X., Bai, J.-M., Zhang, Z.-X., et al. 2019, *ApJ*, 887, 135
- Maoz, D., Netzer, H., Leibowitz, E., et al. 1990, *ApJ*, 351, 75. doi:10.1086/168445
- Martínez-Aldama, M. L., Czerny, B., Kawka, D., et al. 2019, *ApJ*, 883, 170
- Marziani, P., Sulentic, J. W., Zwitter, T., et al. 2001, *ApJ*, 558, 553
- Marziani, P. & Sulentic, J. W. 2014, *MNRAS*, 442, 1211
- Masci, F. J., Laher, R. R., Rusholme, B., et al. 2019, *PASP*, 131, 018003
- Mejía-Restrepo, J. E., Lira, P., Netzer, H., et al. 2018, *Nature Astronomy*, 2, 63
- Pei, L., Fausnaugh, M. M., Barth, A. J., et al. 2017, *ApJ*, 837, 131
- Peterson, B. M. 2014, *SSRv*, 183, 253
- Peterson, B. M., Berlind, P., Bertram, R., et al. 2002, *ApJ*, 581, 197
- Peterson, B. M., Ferrarese, L., Gilbert, K. M., et al. 2004, *ApJ*, 613, 682
- Peterson, B. M. 1993, *PASP*, 105, 247
- Peterson, B. M. & Wandel, A. 1999, *ApJL*, 521, L95
- Peterson, B. M. & Wandel, A. 2000, *ApJL*, 540, L13
- Peterson, B. M., Wanders, I., Horne, K., et al. 1998, *PASP*, 110, 660
- Planck Collaboration, Aghanim, N., Akrami, Y., et al. 2020, *A&A*, 641, A6
- Rodríguez-Pascual, P. M., Alloin, D., Clavel, J., et al. 1997, *ApJS*, 110, 9
- Schlafly, E. F., & Finkbeiner, D. P. 2011, *ApJ*, 737, 103
- Shakura, N. I. & Sunyaev, R. 1973, *A&A*, 24, 337
- Shappee, B. J., Prieto, J. L., Grupe, D., et al. 2014, *ApJ*, 788, 48
- Shen, Y. & Ho, L. C. 2014, *Nature*, 513, 210
- Shen, Y., Horne, K., Grier, C. J., et al. 2016, *ApJ*, 818, 30
- Shen, Y., Richards, G. T., Strauss, M. A., et al. 2011, *ApJS*, 194, 45
- Sulentic, J. W., Marziani, P., & Dultzin-Hacyan, D. 2000, *ARA&A*, 38, 521
- Sulentic, J., Marziani, P., & Zamfir, S. 2011, *Baltic Astronomy*, 20, 427
- van Groningen, E., & Wanders, I. 1992, *PASP*, 104, 700
- Vanden Berk, D. E., Wilhite, B. C., Kron, R. G., et al. 2004, *ApJ*, 601, 692
- Veilleux, S. & Osterbrock, D. E. 1987, *ApJS*, 63, 295
- Wang, J.-M., Du, P., Li, Y.-R., et al. 2014a, *ApJL*, 792, L13
- Wang, J.-M., Du, P., Valls-Gabaud, D. & Netzer, H. 2013, *PhRvL*, 110, 081301
- Wang, J.-M., Qiu, J., Du, P., et al. 2014b, *ApJ*, 797, 65
- Wang, J.-M., Szusszkiewicz, E., Zhou, Y.-Y. & Lu, F.-J. 1999b, *ApJ*, 522, 839
- Wang, J.-M. & Zhou, Y.-Y. 1999a, *ApJ*, 516, 420
- Yu, L.-M., Bian, W.-H., Wang, C., et al. 2019, *MNRAS*, 488, 1519
- Zhang, Z.-X., Du, P., Smith, P. S., et al. 2019, *ApJ*, 876, 49
- Zu, Y., Kochanek, C. S., & Peterson, B. M., 2011, *ApJ*, 735, 80